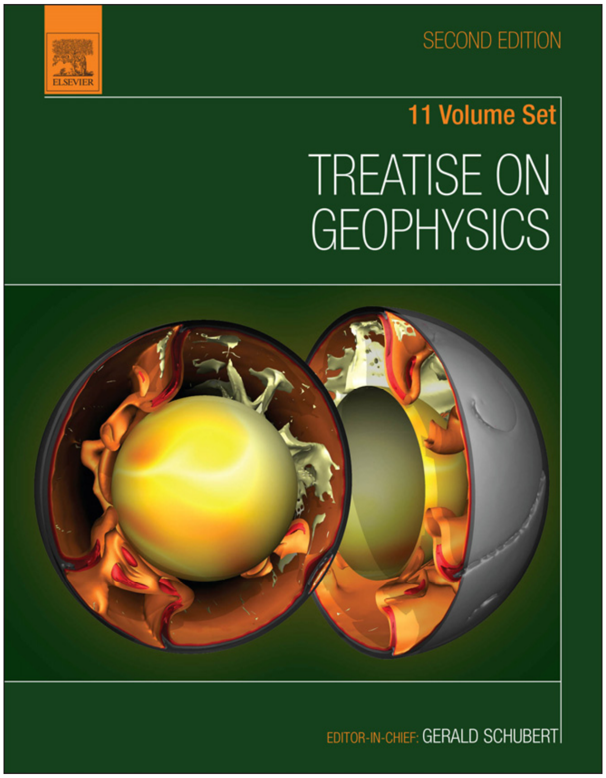

Constable S Geomagnetic Induction Studies. In: Gerald Schubert (editor-in-chief)
Treatise on Geophysics, 2nd edition, Vol 5. Oxford: Elsevier; 2015. p. 219-254.

5.07 Geomagnetic Induction Studies

S Constable, University of California San Diego, La Jolla, CA, USA

http://dx.doi.org/10.1016/B978-0-444-53802-4.00101-9

*Treatise on Geophysics, 2nd edition, (*2015), vol. 5, pp. 219-254

5.07.1 Geomagnetic Induction Studies

The interaction of temporal fluctuations in the Earth's external magnetic field with the electrically conductive rocks of the planet generates internal secondary electric and magnetic fields. The measurements of the primary and secondary fields may then be used to probe the conductivity structure over depths from a few meters to the lower mantle. Conductivity in turn may be used to infer physical and chemical properties, such as temperature, melt content, water and volatile content, mineral type, and anisotropic fabric. There are three basic steps necessary to obtain useful information from geomagnetic induction studies: the estimation of electromagnetic impedances from observations of the electric and magnetic fields, the modeling of these impedances in both forward (conductivity to impedance) and inverse (impedance to conductivity) directions, and, finally, the use of laboratory studies to relate conductivity to the relevant physical and chemical properties. Each of these steps represents significant scientific challenges, and all of them are the subject of current research and recent progress. Clearly, the results of each of these components depend on the quality of the preceding step, and conclusions about the state of the Earth's interior depend on the reliability of all three parts of the process.

Electromagnetic induction covers a very broad field that includes applications in exploration, environmental and mining geophysics, and studies of the Earth's deep interior. Although many of the underlying principles span the entire range of applications, in the context of *Treatise on Geophysics*, we will concentrate on the 'whole-Earth' aspects of geomagnetic induction. For a good discussion of exploration and crustal applications, the reader is referred to the book by Simpson and Bahr (2005).

5.07.1.1 Historical Beginnings

The history of geophysical electromagnetic induction is entwined with the development of the fundamental physics of electromagnetic energy, closely following Oersted's 1820 observation that an electric current deflected a magnet and Ampere's quantification of this phenomenon in the 1820s. Ampere also noted that an electric current exerts a force on a second electric current and that a coil behaved like a magnetic dipole. In 1831, Faraday observed that moving a magnet through a coil produces an electric current, and in 1832, he predicted that water moving through a magnetic field should produce an electric field, an effect that was observed by the British Admiralty much later in 1918.

Induction effects associated with magnetic storms were first seen in telegraph cables, the storm of 1838 being seen on Norwegian telegraph cables; in telegraph lines in England, spontaneous currents reported by W.H. Barlow (1849); and in an observation by Clement (1859) that the aurora of 29 August disrupted telegraphy. The critical mathematical developments started in 1839 with Gauss' spherical harmonic expansion of the main magnetic field, which allows the separation of internal and external magnetic sources, and later (1864) with Maxwell's equations of electromagnetism. In 1865, the Greenwich Observatory started to observe Earth potentials on 15 km grounded lines.

By early in the twentieth century, the relationship between magnetic activity and Earth currents was well known. Schuster and Lamb (1889) observed the relationship between the diurnal magnetic variation and Earth potentials, and Chapman (1919) inferred that the Earth's interior must be more conductive than crustal rocks and modeled the daily variation with a conductive sphere of smaller radius than the Earth's. Although Chapman and Bartels (1940) lamented that a more quantitative relationship between electric conductivity and magnetic field variation was not yet available, progress in this direction was being made. Lahiri and Price (1939) modeled the internal and external parts of the magnetic field using a radial conductivity profile to a depth of nearly 1000 km. Later, Banks (1969) proposed that the harmonics of the 27-day solar rotation were dominantly of P_1^0 spherical harmonic geometry, associated with the ring of current in the magnetosphere above the geomagnetic equator, and produced a conductivity profile down to nearly 2000 km. In order to get an estimate of the electric conductivity of the lowermost mantle, McDonald (1957) modeled the outward propagation of an inferred geomagnetic secular variation signal originating in the core. **Figure 1** summarizes the results of this early work.

These observations represent the beginnings of the geomagnetic depth-sounding (GDS) method, in which magnetic fields alone are used to probe the Earth's conductivity. Another highly important method, magnetotelluric (MT) sounding, began in the early 1950s when Tikhonov (1950) and Cagniard (1953) quantified the relationship between induced electric currents and the magnetic field. Both the GDS and MT methods are in extensive use today, and we will discuss them in this chapter.

5.07.1.2 The Earth's Geomagnetic Environment

Temporal variations in the Earth's magnetic field exist on all timescales from radio frequencies to the reversal record

(Figure 2). Electromagnetic induction methods can exploit only those fields that are externally generated, which in principle means periods shorter than about 1 year for GDS methods (with the possible exception of the 11-year sunspot cycle) and, because the induced electric field components become smaller as period increases, periods of a few weeks or shorter for MT methods. As mentioned in Section 5.07.1, the propagation of internally generated fields of the secular variation upward through the mantle may be used to estimate conductivity (Alexandrescu et al., 1999; McDonald, 1957; Pinheiro and Jackson, 2008), but the lack of an independent estimate of the source-field timing limits this approach (Backus, 1983).

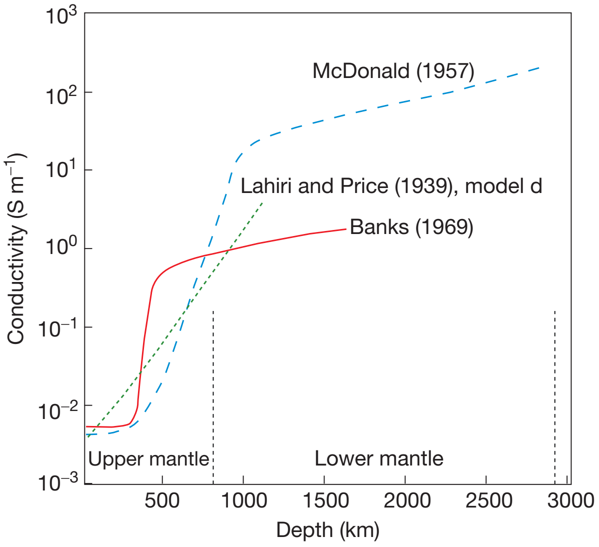

Figure 1 Early electric conductivity profiles of the Earth. These models all feature an increase in conductivity at about the upper/lower mantle transition, a feature of most modern models.

5.07.1.3 Earth/ionosphere cavity

Starting at the high-frequency end of the spectrum, the conductive ionosphere and the conductive Earth are separated by the resistive atmosphere to form a cavity. The electric conductivity of the ground is of order 10^{-3} S m^{-1}, while the atmosphere near the Earth's surface is about 10^{-14} S m^{-1}. What little conductivity there is results from the ionization of oxygen and nitrogen by cosmic rays. The mean free path of these ions increases with decreasing atmospheric density, and by an altitude of 100 km, the start of the ionosphere, conductivity is about the same as that of the solid Earth. The ionosphere is several hundred kilovolts positive with respect to ground, and a leakage current of about 1000 A flows between the ionosphere and ground through an integrated transverse resistance of about 200 Ω. This leakage current supports a vertical electric field of 100–300 V m^{-1} at the ground's surface. The Earth/atmosphere/ionosphere acts as a large capacitor with a value of about 1 F and a time constant of a few thousand seconds. Thus, there must be a return current to sustain the charge on the ionosphere.

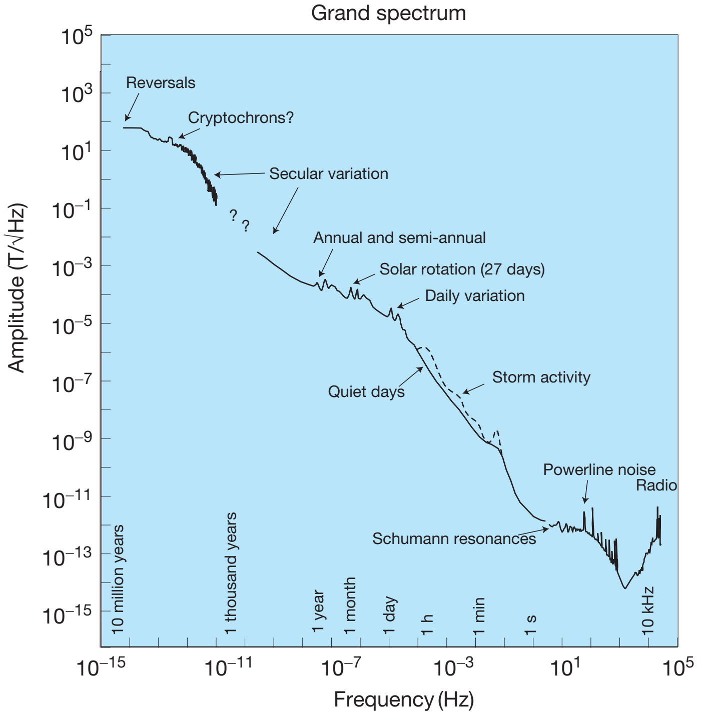

Figure 2 An approximate amplitude spectrum for the Earth's magnetic field (to get a power spectrum, double the exponents, and change the units to T^2/Hz). While somewhat schematic, this figure illustrates that the source and morphology of the field variations depend on frequency. In particular, at periods shorter than about a year, the field is dominated by sources external to the Earth. Reproduced from Constable CG and Constable SC (2004a) Satellite magnetic field measurements: Applications in studying the deep Earth. In: Sparks RSJ and Hawkesworth CT (eds.) *The State of the Planet: Frontiers and Challenges in Geophysics*, *Geophys. Mono. 150*, pp. 147–159. Washington, DC: American Geophysical Union.

The major contributor to the return current is thunderstorm activity, in which convection carries positively charged particles to the tops of thunderclouds and cloud-to-ground negative charge flow in lightning completes the circuit. Thunderstorms preferentially form in the tropics, in the afternoon, and over land. Since Africa is the dominant equatorial land mass, there is an uneven temporal distribution of lightning activity that peaks as the Earth rotates through afternoon in equatorial Africa, or about 16:00 UT. This recharging of the global capacitor can be seen as an increased fair-weather electric field over the oceans anywhere in the world at these times, first observed from the research vessel Carnegie and now known as the Carnegie curve.

The atmospheric cavity is excited by lightning strikes and resonates with a characteristic frequency of about 8 Hz and harmonics, a phenomenon called the Schumann resonance. Man-made sources of electromagnetic energy such as power-line noise at 50 and 60 Hz and the entire radio frequency spectrum also propagate within the resistive atmosphere (Figure 3).

5.07.1.4 Daily variation and Sq

The dayside ionosphere, heated by the sun, is more conductive than the nightside and has a pattern of two circulating current systems (one in each hemisphere) that are stationary in solar time, with an intensified, normally eastward-flowing current at the magnetic equator called the equatorial electrojet. Since the Earth rotates beneath these current systems, a daily variation in magnetic field is seen at the surface of the Earth, amounting to a few tens of nanotesla.

5.07.1.5 The magnetospheric ring current

The largest component of external field variations comes from a ring of current circulating roughly around the magnetic equator at a distance of 2–9 Earth radii. The solar wind injects charged particles into the ring current, mainly positively charged oxygen ions. Sudden increases in the solar wind associated with coronal mass ejections cause magnetic storms, characterized by a sudden commencement, a small but sharp increase in the magnetic field associated with the sudden increased pressure of the solar wind on the Earth's magnetosphere. Following the commencement is a period of fluctuating magnetic field called the initial phase. The main phase of the storm is associated with a large decrease in the magnitude of the fields as a westward circulating ring current is energized – the effect is to cancel the Earth's main dipole field slightly. Finally, there is a recovery phase in which the field returns quasi-exponentially back to normal. All this can happen in a couple of hours or may last days for a large storm.

Although complicated in detail, the ring current behaves somewhat like a large single turn of wire around the Earth, creating fields at the Earth's surface of predominantly simple P_1^0 spherical harmonic geometry. The frequency content is huge: from minute-by-minute fluctuations during a storm, the hours-long duration of a storm, a large peak at the 27-day rotation period of the sun (and harmonics), a semiannual

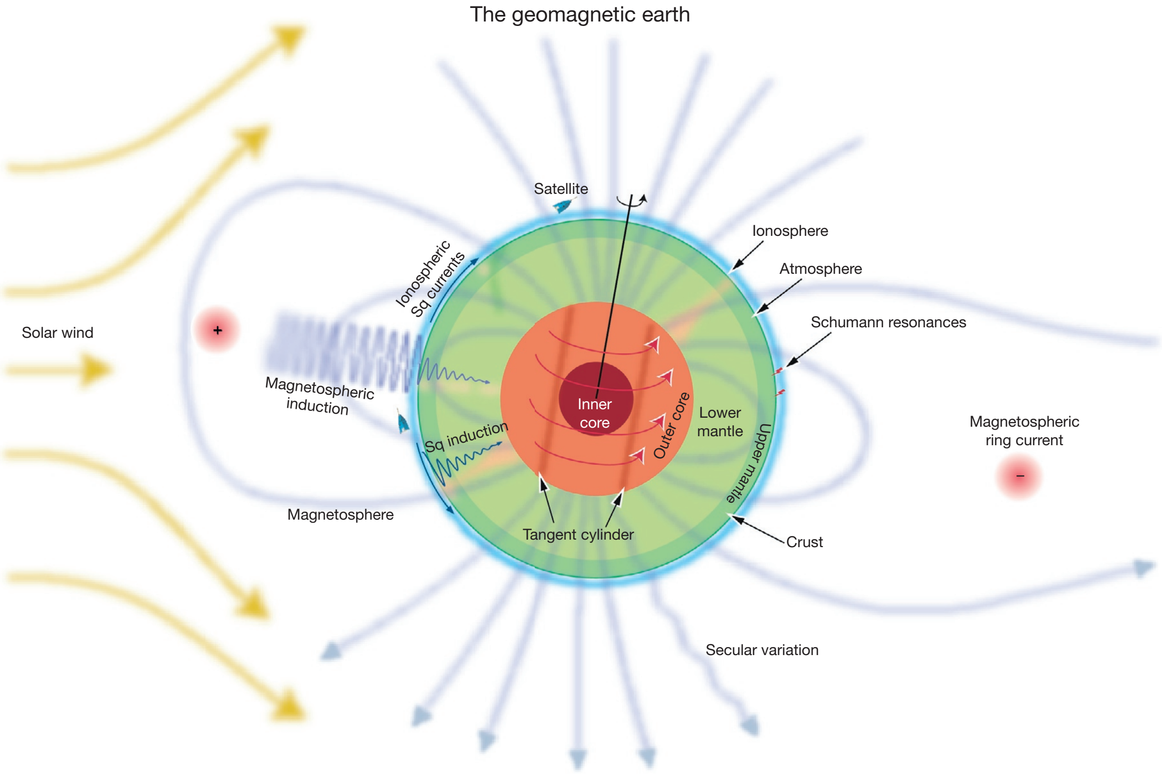

Figure 3 A pictorial representation of the electromagnetic environment of the Earth. Reproduced from Constable CG and Constable SC (2004a) Satellite magnetic field measurements: Applications in studying the deep Earth. In: Sparks RSJ and Hawkesworth CT (eds.) *The State of the Planet: Frontiers and Challenges in Geophysics*, *Geophys. Mono. 150*, pp. 147–159. Washington, DC: American Geophysical Union.

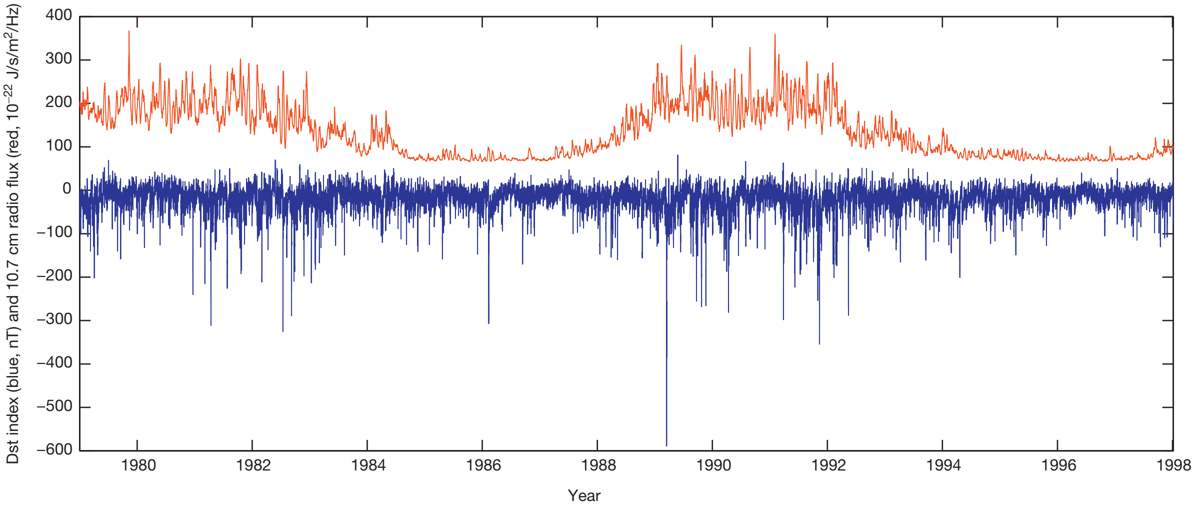

Figure 4 A record of the Dst index (blue) for 19 years between 1979 and 1998. The large negative spikes are individual magnetic storms. To illustrate the relationship between storm activity and the 11-year sunspot cycle, the 10.7 cm solar radio flux is plotted in red.

line associated with the geometry of the ecliptic and the sun's equatorial plane, and, finally, the 11-year solar cycle.

The strength of the ring current is characterized by the 'Dst' (disturbance storm time) index, an index of magnetic activity derived from a network of low- to midlatitude geomagnetic observatories that measures the intensity of the globally symmetrical part of the equatorial ring current (Figure 4). The current method for computing Dst is described in IAGA Bulletin No. 40, a report by Masahisa Sugiura that presents the values of the equatorial Dst index for 1957–86. Honolulu, Hermanus, San Juan, and Kakioka are the currently contributing observatories. The actual morphology of the ring current fields is asymmetrical about the day/night hemisphere, as injection of ions occurs preferentially as a function of solar time (e.g., Balasis and Egbert, 2006).

5.07.1.6 Pulsations

The interaction of the solar wind and magnetosphere can generate resonances and waves that have relatively narrowband frequency content, creating quasiperiodic oscillations of the magnetic field called pulsations. The period of oscillation varies between about 1 s and several hundred seconds, and the nomenclature for pulsations distinguishes between various frequency bands and whether the variations are continuous for a time or form a damped oscillation (see Parkinson, 1983).

5.07.2 Geomagnetic Sounding

5.07.2.1 Introductory Theory

One of the key concepts in geomagnetic induction is that of the *skin depth*, the characteristic length over which electromagnetic fields attenuate. We can derive the skin depth starting with Faraday's law

$$\nabla \times \mathbf{E} = -\frac{\partial \mathbf{B}}{\partial t}$$

and Ampere's law

$$\nabla \times \mathbf{H} = \mathbf{J}$$

where **J** is the current density (A m^{-2}), **E** is the electric field (V m^{-1}), **B** is the magnetic flux density or induction (T), and **H** is the magnetic field intensity (A m^{-1}). We neglect displacement currents, as they are not significant at the frequencies and conductivities relevant to geomagnetic induction (for a rigorous justification of this, see Section 2.4 of Backus et al., 1996). We can use the identity $\nabla \bullet \nabla \times \mathbf{A} = 0$ to show that

$$\nabla \times \mathbf{B} = 0 \text{ and } \nabla \times \mathbf{J} = 0$$

in regions free of sources of magnetic fields and currents. **B** and **H** are related by magnetic permeability μ and **J** and **E** by conductivity σ

$$\mathbf{B} = \mu \mathbf{H} \qquad \mathbf{J} = \sigma \mathbf{E}$$

(the latter equation is Ohm's law), and so

$$\nabla \times \mathbf{E} = -\mu \frac{\partial \mathbf{H}}{\partial t}$$
$$\nabla \times \mathbf{H} = \sigma \mathbf{E}$$

If we take the curl of these equations and use $\nabla \times (\nabla \times \mathbf{A}) = \nabla(\nabla \bullet \mathbf{A}) - \nabla^2 \mathbf{A}$, for constants σ and μ, we have

$$\nabla^2 \mathbf{E} = \mu \frac{\partial}{\partial t}(\nabla \times \mathbf{H}) = \mu\sigma \frac{\partial \mathbf{E}}{\partial t}$$
$$\nabla^2 \mathbf{H} = \sigma(\nabla \times \mathbf{E}) = \mu\sigma \frac{\partial \mathbf{H}}{\partial t}$$

which are diffusion equations. In air and very poor conductors where $\sigma \approx 0$, or if $\omega = 0$, the equations reduce to Laplace's equation. Now, if we consider sinusoidally varying fields of angular frequency ω,

$$\mathbf{E}(t) = \mathbf{E}_o e^{i\omega t} \qquad \frac{\partial \mathbf{E}}{\partial t} = i\omega \mathbf{E}$$
$$\mathbf{H}(t) = \mathbf{H}_o e^{i\omega t} \qquad \frac{\partial \mathbf{H}}{\partial t} = i\omega \mathbf{H}$$

and so

$$\nabla^2 \mathbf{E} = i\omega\mu\sigma \mathbf{E}$$
$$\nabla^2 \mathbf{H} = i\omega\mu\sigma \mathbf{H}$$

If we further consider fields that are horizontally polarized in the *xy* directions and are propagating vertically into a half-space, in Cartesian coordinates, these equations decouple to

$$\frac{\partial^2 \mathbf{E}}{\partial z^2} + k^2 \mathbf{E} = 0$$

$$\frac{\partial^2 \mathbf{H}}{\partial z^2} + k^2 \mathbf{H} = 0$$

with solutions

$$\begin{aligned} \mathbf{E} &= \mathbf{E}_o e^{-ikz} = \mathbf{E}_o e^{-i\alpha z} e^{-\beta z} \\ \mathbf{H} &= \mathbf{H}_o e^{-ikz} = \mathbf{H}_o e^{-i\alpha z} e^{-\beta z} \end{aligned}$$

where we have defined a complex wave number

$$k = \sqrt{i\omega\mu\sigma} = \sigma - i\beta$$

and an attenuation factor, which is called a skin depth,

$$z_s = 1/\alpha = 1/\beta = \sqrt{\frac{2}{\sigma\mu_o\omega}}$$

The skin depth is the distance that field amplitudes are reduced to $1/e$, or about 37%, and the phase progresses one radian, or about 57°. In practical units of meters, the skin depth is

$$z_s \approx 500\sqrt{1/\sigma f}$$

where circular frequency f is defined by $\omega = 2\pi f$.

The skin depth concept underlies all of inductive electromagnetism in geophysics. Substituting a few numbers into the equation shows that skin depths cover all geophysically useful length scales from less than a meter for conductive rocks and kilohertz frequencies to thousands of kilometers in mantle rocks and periods of days (Table 1). Skin depth is a reliable indicator of maximum depth of penetration, but one should not think of skin depth as a resolution length. A thin conductive layer can have an effect at periods associated with skin depths much larger than its width, and all external magnetic field variations have to propagate through surface layers. The skin depth describes attenuation associated with induction, but electric and magnetic fields are also modified by variations in conductivity through Ohm's law even in the DC limit, an effect often described as 'galvanic' rather than inductive.

5.07.2.2 The MT Method

Because the skin depth generates a natural scale length for time-varying fields, the response of the Earth to time variations in the externally generated geomagnetic field can be interpreted in terms of electric conductivity with depth. The estimation of purely geomagnetic response functions and their interpretation in terms of mantle electric conductivity structure date from the end of the nineteenth century, but the additional use of electric field measurements only started with Cagniard's work in the 1950s.

One can see that the core is effectively a perfect conductor into which even the longest-period external magnetic field cannot penetrate. However, 1-year variations can penetrate into the lower mantle. The very large range of conductivities found in the crust (sea, sediment, and igneous rock) indicates the need for a corresponding large range of frequencies in electromagnetic sounding of that region.

Continuing with our half-space formulation, we can define an impedance by taking the ratio of orthogonal field components

$$z = \frac{E_x}{H_y} = \frac{\mu\omega}{k}$$

where we recall that the complex wave number

$$k = \alpha - i\beta = (\sigma\mu\omega)^{\frac{1}{2}} e^{-i\frac{\pi}{4}}$$

and so we can see that E_x leads H_y by 45° and that the half-space resistivity is given by

$$\rho = \frac{1}{\sigma} = \frac{1}{2\pi f\mu}|Z|^2 = \frac{T}{2\pi\mu}\left|\frac{E_x}{H_y}\right|^2$$

for fields with period T. This is the MT formula made famous by Cagniard (1953). Perhaps more usefully (since measurements tend to be made in **B** rather than **H**),

$$\rho = \frac{\mu}{\omega}\left|\frac{E_x}{B_y}\right|^2$$

Another quantity called the c-response (Weidelt, 1972) (also called admittance by Parker, 1994) is also used, given by

$$c = -\frac{E_x}{i\omega B_y}$$

(note that c is complex) from which it can be seen that

$$\rho = \omega\mu|c|^2$$

If the Earth really were a homogeneous half-space, the resistivity obtained at all periods would be the same and equal to the true resistivity of the Earth, and the phase between **B** and **E** would be constant at 45°. Of course, this is never the case, but resistivities are computed nevertheless and described as 'apparent resistivities.' Solutions for computing the apparent

Table 1 Approximate skin depths for a variety of typical Earth environments and a large range of frequencies

Material	*σ (S m^{-1})*	*1 year*	*1 month*	*1 day*	*1 h*	*1 s*	*1 ms*
Core	5×10^5	4 km	1 km	209 m	43 m	71 cm	23 mm
Lower mantle	10	894 km	258 km	47 km	9 km	160 m	5 m
Seawater	3	1600 km	470 km	85 km	17 km	290 m	9 m
Sediments	0.1	9000 km	2600 km	470 km	95 km	1.6 km	50 m
Upper mantle	0.01	3×10^4 km	8000 km	1500 km	300 km	5 km	160 m
Igneous rock	1×10^{-5}	10^6 km	2×10^5 km	5×10^4 km	9500 km	160 km	5 km

resistivity response of layered 2D and even 3D models exist and are used to interpret the MT data. The phase relationship between *E* and *B* is also estimated and is useful because it is independent of the amplitudes of *E* and *H*. Complicated near-surface structure can change the amplitude of the electric fields very easily, but because these distortions are not inductive, the phase relationships are not altered.

5.07.2.3 MT in Practice

Figure 5(a) shows a schematic layout of an MT measurement; the magnetic and electric fields are measured orthogonal to each other. To a first approximation, the magnetic field is the EM source and the electric field is the EM response. For a 1D Earth, this would be the only measurement required; for a 2D or 3D Earth, measurements are made in both directions, and perhaps, even the vertical magnetic field would be measured. In Figure 5(b), we provide a quantitative example of this behavior, plotting magnetic field, electric field, and current density for 0.5 Hz energy propagating into a model containing a buried conductive layer. All the fields decay quasi-exponentially within the Earth, but inside the conductor, the magnetic fields can be seen to attenuate more rapidly due to induced electric currents, which peak inside this layer. At a higher frequency (5 Hz), magnetic fields attenuate before the conductive layer is reached because of the shorter skin depth. Without the conductive layer, fields propagate more deeply into the Earth, but importantly, the electric field at the surface depends on structure at depth. This is the principle of the MT method.

MT measurements can be made from the low end of the radio frequency spectrum, using radio stations and lightning as sources of energy, to periods of several days. The table of skin depths gives some indication of the relationship between conductivity, period, and penetration scale. Structure can profoundly affect the way MT fields propagate, but skin-effect attenuation provides an indication of the limits to deepest sensitivity (see Figure 5(b)). The type of instrumentation used to record the *E* and *B* fields will depend on the periods required, and the time over which data are collected will determine the longest period available. Horizontal spacing of MT sites can vary from continuous electric field dipoles for shallow crustal studies, to individual sites spaced tens of kilometers apart for regional profiles, to single long-period soundings for mantle conductivity studies (e.g., Egbert and Booker, 1992; Tarits et al., 2004).

5.07.2.4 Equipment

5.07.2.4.1 Electric field measurements

Metal electrodes are too noisy for MT measurements, except at radio frequencies. A nonpolarizing electrode, or porous pot, is almost always used, in which a reversible electrochemical reaction is restricted to that of a single chemistry. Electric connection is made to a metal rod dipped into an aqueous saturated solution of the metal salt (Figure 6). Contact is made with the ground through a semipermeable material such as unglazed porcelain, porous plastic, or plaster. Copper–copper sulfate is a common chemistry for land use, as is lead–lead chloride stabilized in plaster of Paris or mud made with lead chloride solution (Petiau, 2000). (For marine use, silver–silver chloride provides a low-noise electrode, the silver chloride being compatible with seawater and very low solubility (Filloux, 1987; Webb et al., 1985).) On land, such a system produces a low-noise electric contact with an impedance of typically a few kiloohm. Electrodes are buried at a depth of around 30 cm or more to limit temperature variations, which can generate a time-varying potential on the electrode. Dipole lengths are about 50–200 m. Since signals are of order mV km^{-1}, a gain of 10–1000 is applied before digitization. The amplifier needs to be a true differential amplifier because there is no natural concept of 'ground' when making telluric measurements.

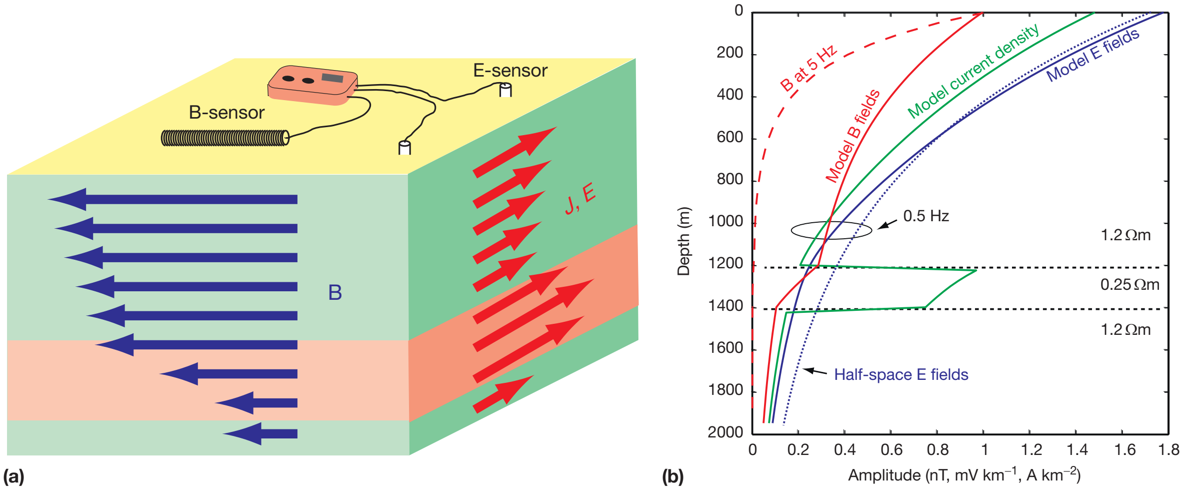

Figure 5 (a) Schematic of an magnetotelluric (MT) measurement. Orthogonal components of the magnetic and electric field are measured at the surface of the Earth. In conductive layers (red), electric fields and currents are induced whose secondary magnetic fields attenuate the primary magnetic field more rapidly than in the background material. (b) In a quantitative example of this behavior, magnetic field, electric field, and current density are plotted for 0.5 Hz energy propagating into a model containing a buried conductive layer (solid lines). For comparison, magnetic fields for a 5 Hz source field are shown (broken red line). The dotted blue line shows the electric fields without the conductive layer.

Often, optical isolation is used to ensure no ground path exists between the recording system and the electrode system.

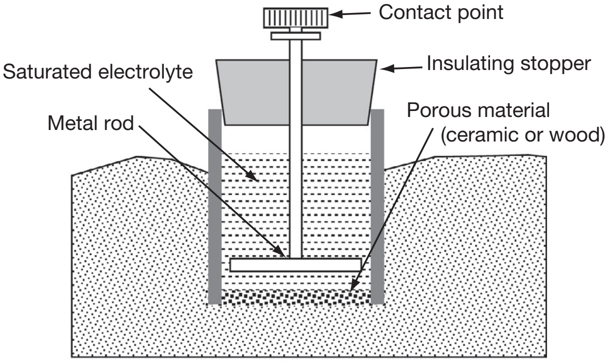

Figure 6 Porous pot, or nonpolarizing, electrode.

5.07.2.4.2 Magnetic field measurements

Two types of magnetic field sensor are in common use, both necessarily vector instruments (which rules out nuclear precession sensors). For periods shorter than a few thousand seconds, induction coils are used, and for periods longer than about 10 s, fluxgate magnetometers provide a lower-noise measurement.

Induction coils (**Figure 7**) are simply an application of Faraday's law

$$\oint_C \mathbf{E}\cdot d\mathbf{l} = -\frac{d\Phi}{dt}$$

so integrating E around a single loop of wire of area A gives a potential difference

$$V = -A\frac{dB}{dt}$$

We see that V increases with frequency, but since variations in B are of order pico- to nanotesla, unless A is huge, this does not produce much of a voltage. Two approaches are used to boost V. The first is to simply wind many (say, N) turns in series and the second is to increase the flux through the coil by inserting a core material of high relative permeability μ_r, such as mumetal or Permalloy. The permeable core provides an effective increase in flux through the coil by a factor of a, so

$$V = -aNA\frac{dB}{dt}$$

The relative permeability of mumetal alloys is of order 10^4–10^5, so a can be made quite high. In practice, a long, thin coil is used because then a is limited by the core geometry, rather than μ_r, thus removing any temperature dependence in μ_r from the sensor. Since most of the flux is trapped in the core material, A becomes the cross-sectional area of the core, rather than the area of each turn of the wire. For large N, achieved by making the windings out of a very fine wire, the dominant source of noise becomes the thermal resistance noise, or Johnson noise, of the wire:

$$V_J^2 = 4kTR$$

where k is the Boltzmann constant ($1.4\times10^{-23}\ \mathrm{J\,K^{-1}}$), T is the temperature, and R is the resistance. Here, we see the second reason for a long, thin magnetometer. Piling windings upon windings increases the diameter of the turns, and so R starts to increase more rapidly than V.

A good induction coil magnetometer has a noise level of about $10^{-8}\ \mathrm{nT^2\,Hz^{-1}}$ at around 1 Hz (i.e., less than a picotesla), with a red noise spectrum at lower frequencies because of the dB/dt loss of sensitivity. Long-period response is limited to about 5000 s, while high-frequency response is limited by capacitive and inductive losses in the core material. This is addressed by laminating the core material and, ultimately, going to air-cored coils for the highest (low radio) frequencies. Because the Earth's main field is around 40 mT, minute rotation of an induction coil magnetometer couples this field into the sensor. For a subpicotesla noise floor, this corresponds to a rotation of only a nanoradian, or 1 mm in 1000 km. For these reasons, coils are buried 10 cm or so to avoid wind motion, and even so MT sites near trees or coastlines will be observed to have high noise levels.

The fluxgate magnetometer (**Figure 8**) measures the total magnetic field and so is useful for long-period MT studies and magnetic observatory recording. In a fluxgate magnetometer, two primary coils are wound around two identical cores of permeable material and connected in series so that a current passed through the primary circuit generates magnetic fields in the two cores that oppose each other. A 50–1000 Hz primary current is used of sufficient strength to saturate the cores. In the absence of an external field, the magnetization in the cores is equal and opposite, so there is no net magnetic field for the two-core system. In the presence of an external field, the core being magnetized in the direction of the external field saturates sooner than the opposite core. Thus, an asymmetry develops in the magnetization of the cores, leading to a time-varying net magnetization. A secondary coil wound around the entire system measures the rate of change of this magnetization as a series of induced voltage spikes. These spikes are rectified and amplified to produce a voltage signal that is proportional to the magnetic field along the axis of the sensor cores. Note that

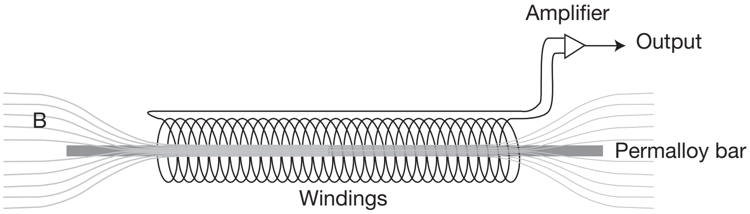

Figure 7 Induction coil magnetometer.

the fundamental harmonic of the sensing voltage is twice the fundamental harmonic of the primary current.

Because permeability and saturation magnetization will depend on temperature, one common approach to building a fluxgate sensor is to operate it as a null instrument. A solenoid around the fluxgate sensor carries an electric current that creates a magnetic field equal and opposite the Earth's field (in that direction). The output of the fluxgate should then be zero (and so need not be calibrated). Any nonzero measurements from the fluxgate are fed back into the solenoid current to return the measurement to zero. The current in the solenoid, rather than the fluxgate output, is then the measurement of the magnetic field. Another common modification is to use a permeable core in the shape of a ring with a toroidal excitation winding. Further details can be found in Nielsen et al. (1995).

Because the main magnetic field is so large (around 40 mT), dynamic range and sensitivity issues limit the noise floor of the fluxgate to about 0.01 nT, and the noise curves of fluxgates and induction coils cross at around 500 s period (see, e.g., Figure 2 of Constable, 2013). However, the noise stays below the geomagnetic spectrum until about 1 Hz, making the fluxgate an adequate induction sensor for periods longer than about 10 s.

5.07.2.5 MT Data Processing

The raw measurements made in the field are time series of magnetic and electric fields, usually in two orthogonal directions. An example is given in Figure 9. The objective of MT data processing is to obtain the frequency domain response of the coherent part of these signals.

The frequency domain transfer function between the horizontal magnetic and electric field is called the MT impedance tensor Z:

$$\begin{bmatrix} E_x(\omega) \\ E_y(\omega) \end{bmatrix} = \begin{bmatrix} Z_{xx}(\omega) & Z_{xy}(\omega) \\ Z_{yx}(\omega) & Z_{yy}(\omega) \end{bmatrix} \begin{bmatrix} H_x(\omega) \\ H_y(\omega) \end{bmatrix}$$

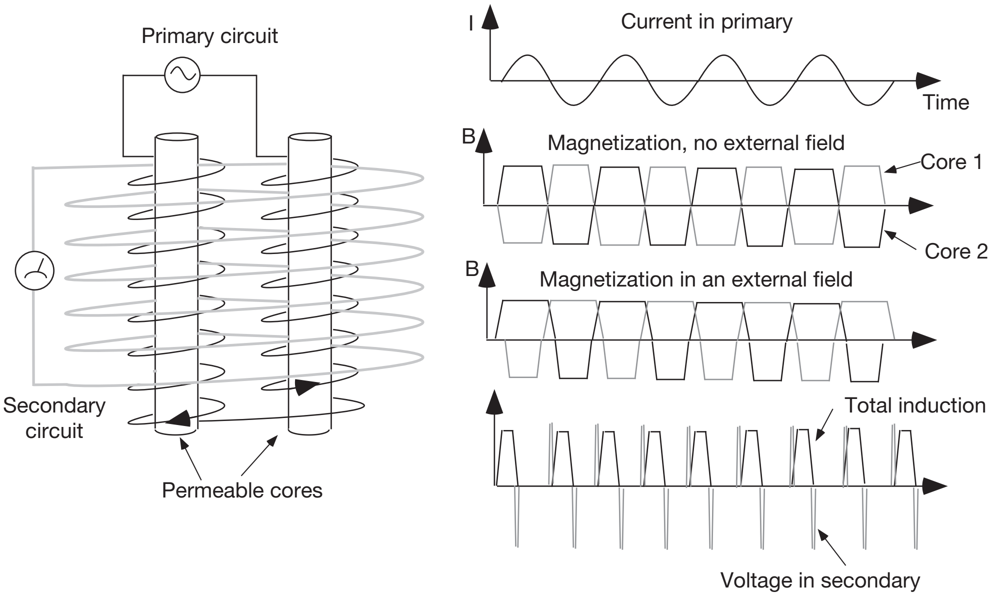

Figure 8 Principle of operation for a fluxgate magnetometer. Two permeable cores are driven into saturation in opposite directions at frequency f. A bias associated with an external field along the axis of the cores produces an asymmetry in the internal fields and a total internal field of frequency $2f$, detected in a secondary winding by a phase-locked amplifier.

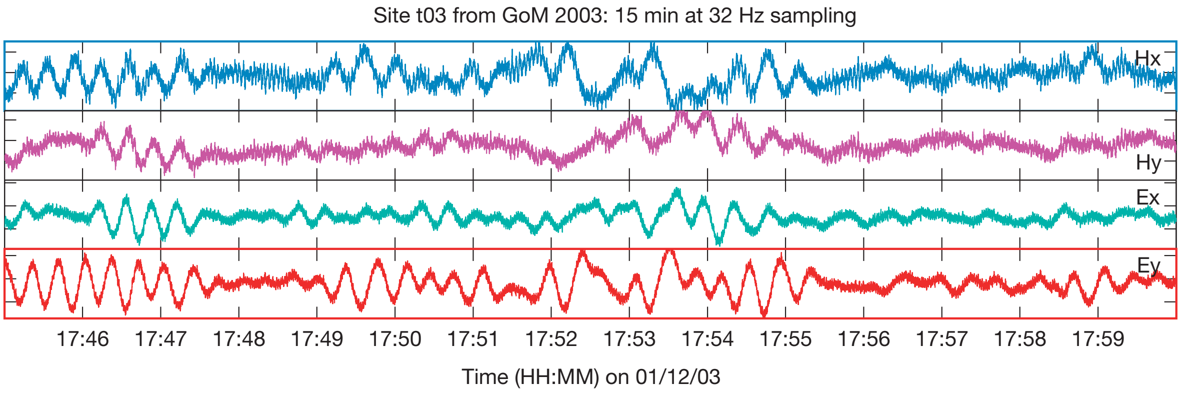

Figure 9 Sample of MT time-series measurements, in arbitrary units. Note that H_x and E_y are anticorrelated, and H_y and E_x are correlated.

(we will drop the ω dependence for clarity). The standard treatment of a transfer function would consider H the input and E the output with noise ϵ in the output measurement only

$$E = ZH + \varepsilon$$

which in the classic least squares approach is estimated by

$$\widehat{Z} = \frac{\langle H^{\dagger}E \rangle}{\langle H^{\dagger}H \rangle}$$

where $\langle H^{\dagger}E \rangle$ is the cross spectrum between H and E. The problem is that there is noise in H and E, which will bias $\langle H^{\dagger}H \rangle$ up and bias Z down. The remote reference technique was introduced (Gamble et al., 1979) to reduce bias associated with noise in H by making a second measurement of the magnetic field, H_r, sufficiently far away (remote) that the noise sources are independent, relying on the fact that the magnetic source field is coherent over very large distances.

Then,

$$\widehat{Z} = \frac{\langle H_{\mathrm{r}}^{\dagger}E \rangle}{\langle H_{\mathrm{r}}^{\dagger}H \rangle}$$

and with any luck, $\langle H_{\mathrm{r}}^{\dagger}H \rangle$ is now unbiased. The least squares method also assumes that noise is normally distributed. Non-Gaussian noise can be handled with an iterative robust weight W

$$\widehat{Z} = \frac{\langle H_{\mathrm{r}}^{\dagger}WE \rangle}{\langle H_{\mathrm{r}}^{\dagger}WH \rangle}$$

which reduces the effect of outliers. Both the effects of non-Gaussian noise and nonstationary source-field spectra can be handled by various robust estimation techniques (e.g., Chave et al., 1987; Egbert and Booker, 1986). These approaches were generalized into an eigenvalue decomposition for multiple MT sites by Egbert (1997).

The nature of Z depends on the apparent dimensionality of the geology:

For 1D, $Z_{xx} = Z_{yy} = 0;\ \ Z_{xy} = -Z_{yx}$
For 2D, $Z_{xx} = Z_{yy} = 0;\ \ Z_{xy} \neq -Z_{yx}$
For 3D, $Z_{xx}, Z_{yy}, Z_{xy}, Z_{yx} \neq 0$.

For 2D structure, $Z_{xx} = Z_{yy} = 0$ only when the coordinate system of the measurement is aligned to the 2D geometry of the geology. With a prior understanding of structural trends or geologic strike, the experimenter will normally arrange for this to be approximately so. Otherwise, the tensor can be rotated mathematically to minimize Z_{xx} and Z_{yy}. Conventionally, the impedance with electric field along strike is called the transverse electric, or TE mode, and the impedance with across-strike electric fields is called the transverse magnetic, or TM mode.

5.07.2.6 Global Conductivity Studies

If one wants to look deep into the Earth using electric techniques and to study the properties of the deeper mantle, then the MT method is not the ideal tool. First, one needs very long time series of the EM fields, spanning perhaps years, and while magnetic observatories have been collecting records for more than a hundred years, there are few observatories collecting electric field data. Secondly, if one examines the MT relationship

$$\rho_{\mathrm{a}} = \frac{T}{2\pi\mu}\left|\frac{E}{B}\right|^2$$

one observes that for a given magnetic field and resistivity, the amplitude of the induced electric field decreases with period

$$E = B\sqrt{\frac{2\pi\mu\rho_{\mathrm{a}}}{T}}$$

which is exacerbated by a falling ρ_{a} with depth and period. At long periods, the assumption that the source-field morphology is uniform over scales comparable to the depth of penetration in the Earth breaks down, particularly for the daily variation and harmonics (e.g., Bahr et al., 1993). Finally, there will be an ambiguity in the absolute value of mantle conductivity associated with unknown static effects in the electric data.

5.07.2.7 Global Response Functions

One can derive other types of electric response functions, similar in nature to the MT response, using only the three components of the magnetic field recorded by geomagnetic observatories (GDS, responses). Much of this work is still based on techniques developed by Banks (1969). **Figure 10** shows an example of overlapping GDS and MT response functions.

The vector magnetic field can be written as a gradient of a scalar potential in the usual fashion

$$\mathbf{B} = -\mu_{\mathrm{o}}\nabla\Omega$$

and, following Gauss, the scalar potential can be expanded in turn into coefficients of internal (i_n) and external (e_n) origin for spherical harmonics P_n:

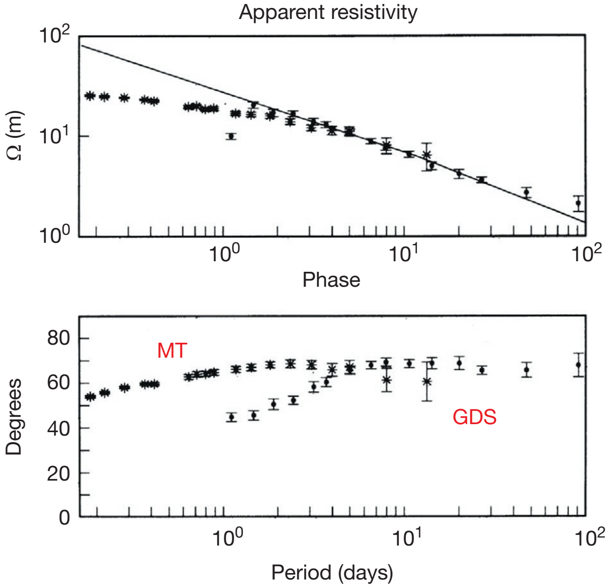

Figure 10 A combination of MT and geomagnetic depth-sounding (GDS) response functions from Egbert and Booker (1992). Magnetotelluric data are available to a maximum of 10-day period (about 10^6 s), while GDS data can extend this to periods of many months.

$$\Omega = a_{\mathrm{o}} \sum_n \left\{ i_n \left(\frac{a_{\mathrm{o}}}{r}\right)^{n+1} + e_n \left(\frac{r}{a_{\mathrm{o}}}\right)^n \right\} P_n(\cos\theta)$$

where n is the degree of spherical harmonic, a_{o} is the radius of the Earth, θ is geomagnetic colatitude, and r is the radius of observation. If one chooses geomagnetic coordinates, then the analysis is zonal in terms of the main dipole field. The i_n and e_n can be functions of time or frequency although, like MT, this kind of analysis is usually done in the frequency domain.

One can thus define a geomagnetic response for a radially symmetrical Earth as simply the ratio of induced (internal) to external fields:

$$Q_n(\omega) = \frac{i_n(\omega)}{e_n(\omega)}$$

where the frequency domain is again made explicit and will be implicit in the following.

In certain circumstances, such as satellite observations, one has enough data to fit the e_n and i_n directly. However, most of the time, one just has horizontal (H) and vertical (Z) components of **B** as recorded by a single observatory. We can obtain H and Z from the appropriate partial derivatives of Ω to obtain

$$\begin{aligned} H &= \mu_{\mathrm{o}} \left(\frac{1}{r}\frac{\partial\Omega}{\partial\theta}\right)_{r=a_{\mathrm{o}}} \\ &= \mu_{\mathrm{o}} \sum_n A_{H,n} \frac{\partial P_n(\cos\theta)}{\partial\theta} \end{aligned}$$

and

$$\begin{aligned} z &= \mu_{\mathrm{o}} \left(\frac{\partial\Omega}{\partial r}\right) r = a_{\mathrm{o}} \\ &= \mu_{\mathrm{o}} \sum_n A_{Z,n} P_n(\cos\theta) \end{aligned}$$

where we have defined new expansion coefficients

$$\begin{aligned} A_{H,n} &= i_n + e_n \\ A_{Z,n} &= n e_n + (n+1) i_n \end{aligned}$$

Thus, we can define a new electromagnetic response

$$W_n = \frac{A_{Z,n}}{A_{H,n}}$$

related to Q by

$$Q_n = \frac{i_n}{e_n} = \frac{n - A_{Z,n}/A_{H,n}}{n + 1 + A_{Z,n}/A_{H,n}}$$

The inductive scale length or c-response is, in turn,

$$c_n = \frac{a_{\mathrm{o}} W_n}{n(n+1)}$$

where the MT apparent resistivity and phase are

$$\rho_{\mathrm{a}} = \omega\mu_{\mathrm{o}} |i c_n|^2 \qquad \phi = \arg(\omega\mu_{\mathrm{o}} i c_n)$$

Note that for causal systems, the real part of c is positive, and the imaginary part is always negative.

Banks showed that the previously mentioned analysis could be simplified because, except for the daily and annual variations, the magnetic field was dominantly of P_1^0 geometry as a result of the nature of the ring current.

If one can assume a simple degree-one field geometry, the earlier-mentioned discussion of response functions simplifies greatly. W becomes simply the ratio of vertical to horizontal fields with a colatitudinal trigonometric term. The c-response becomes simply $c = a_{\mathrm{o}} W/2$. Banks looked at the geometry of simultaneous observatory records as a function of geomagnetic colatitude to demonstrate the P_1^0 geometry. Having shown this, one can take records from a single observatory and, assuming P_1^0, compute a geomagnetic response function. Since some observatories have been recording for over a hundred years, this allows response functions to be computed out to periods of at least 6 months.

The daily variation Sq and harmonics can also be used to infer geomagnetic response functions, but this is proportionately more difficult because of the more complicated geometry of the source fields. The nature of the source field cannot be assumed a priori, but rather must be estimated using an array of observatory sites. For example, Olsen (1992) used nearly 100 observatories and a spherical harmonic representation of degree 10 to estimate geomagnetic responses for the first 6 daily harmonics.

5.07.2.7.1 Using magnetic satellites

The use of magnetic satellites to examine global induction potentially allows the continents and oceans to be examined together. Because satellites sample the entire Earth, one can transcend the limitations of the sparse and uneven observatory distribution and also sample source-field morphology better than for a single-site GDS measurement (although simultaneous processing of data from the global observatory network would sample the source field better than a single satellite could; e.g., Balasis and Egbert, 2006, in practice the observatories are often processed individually). However, because satellites move through the static parts of the Earth's magnetic field, folding spatial variations into temporal variations within the satellite frame of reference, considerable effort is required to remove the Earth's main field, secular variation, crustal field, and daily variation/equatorial electrojet (if one wishes to process only ring current induction). One tool that attempts to model all these phenomena simultaneously is the comprehensive model (Sabaka et al., 2004). Even so, it is difficult to remove the effects of field-aligned currents in the auroral zones, and so data are typically processed between ±50° geomagnetic latitude, and residual effects of the daily variation are usually avoided by using only nighttime data.

To obtain response functions from satellite data after removal of nonmagnetospheric effects, we return to our spherical harmonic expansion of associated Legendre polynomials P_l^{m}, with Schmidt quasi-normalized spherical harmonic coefficients representing the internal $i_l^{\mathrm{m}}(t)$ and external $e_l^{\mathrm{m}}(t)$ magnetic fields as a function of time t:

$$\Phi(r,\theta,\phi) = a_{\mathrm{o}} \sum_{l=1}^{\infty} \sum_{m=-l}^{l} \left\{ i_l^{\mathrm{m}}(t) \left(\frac{a_{\mathrm{o}}}{r}\right)^{l+1} + e_l^{\mathrm{m}}(t) \left(\frac{r}{a_{\mathrm{o}}}\right)^{l} \right\} P_l^{\mathrm{m}}(\cos\theta) \mathrm{e}^{im\phi}$$

Keeping only the P_1^0 contribution and with r, θ, ϕ in geomagnetic coordinates

$$\Phi_1^0(r,\theta) = a_o\left\{i_1^0(t)\left(\frac{a_o}{r}\right)^2 + e_1^0(t)\left(\frac{r}{a_o}\right)\right\}P_1^0(\cos\theta)$$

and so the magnetic induction **B** is derived from the negative of the gradient in the usual manner

$$\mathbf{B}(r,\theta,\phi) = -\nabla\Phi_1^0(r,\theta,\phi)$$

or expressed as components B_r, B_θ, B_ϕ of a spherical coordinate system:

$$B_r = \left[-e_1^0 + 2i_1^0\left(\frac{a}{r}\right)^3\right]\cos(\theta)$$

$$B_\theta = \left[e_1^0 + i_1^0\left(\frac{a}{r}\right)^3\right]\sin(\theta)$$

$$B_\phi = 0$$

For an analysis using a single satellite, these equations can be fit to data from each equatorial pass having different values of altitude (r) and geomagnetic colatitude (θ), as was done by Didwall (1984) in the first analysis of POGO data, and subsequent studies by Olsen et al. (2003) and Constable and Constable (2004b), providing estimates of $i_1^0(t)$ and $e_1^0(t)$ at about 100 min intervals. For studies using multiple satellites (e.g., Kuvshinov and Olsen, 2006; Olsen et al., 2003), a parameterized fit to higher-order coefficients can be made. These time series may then be Fourier transformed into the frequency domain to derive a complex geomagnetic response function of frequency:

$$Q_1^0(\omega) = i_1^0(\omega)/e_1^0(\omega)$$

Figure 11 provides a comparison of several satellite GDS responses.

5.07.3 Interpretation of GDS and MT Data

The subjects of this section are the mechanisms by which one can relate MT and GDS response functions to electric conductivity distributions in the Earth. Predicting the response functions that would be observed over a given conductivity model is the 'forward problem,' and estimating conductivity from response function data is the 'inverse problem.'

5.07.3.1 Forward Model Studies

If the forward modeling computation is fast enough, and the models simple enough, then it is perfectly reasonable to guess a conductivity model, compute and compare the predicted response to the data visually, and estimate ways in which the model needs to be modified to improve the fit. Forward modeling requires some understanding of how variations in the model affect the predicted data but allows geologic prejudices to be incorporated directly into the process. This approach can be automated through stochastic inversion methods, which test thousands or even millions of models for compatibility with the data and derive statistical properties of the acceptable model space. Because it is extremely inefficient to test truly random models (using Monte Carlo methods), various schemes are used to generate models, such as simulated annealing (e.g., Dosso and Oldenburg, 1991), evolutionary or genetic algorithms (e.g., Everett and Schultz, 1993), and Markov chains (e.g., Grandis et al., 1999).

Another role of forward model studies is hypothesis testing. If the number of possible geologic models is limited, and each model is likely to have a distinct geophysical signature, then geophysical models can be built for each hypothesis and computed to see if the predictions are compatible with the observed data.

5.07.3.2 Parameterized Inversion

If it is sensible to approximate the true complexity of geology to a model having only a few parameters, then there is a whole

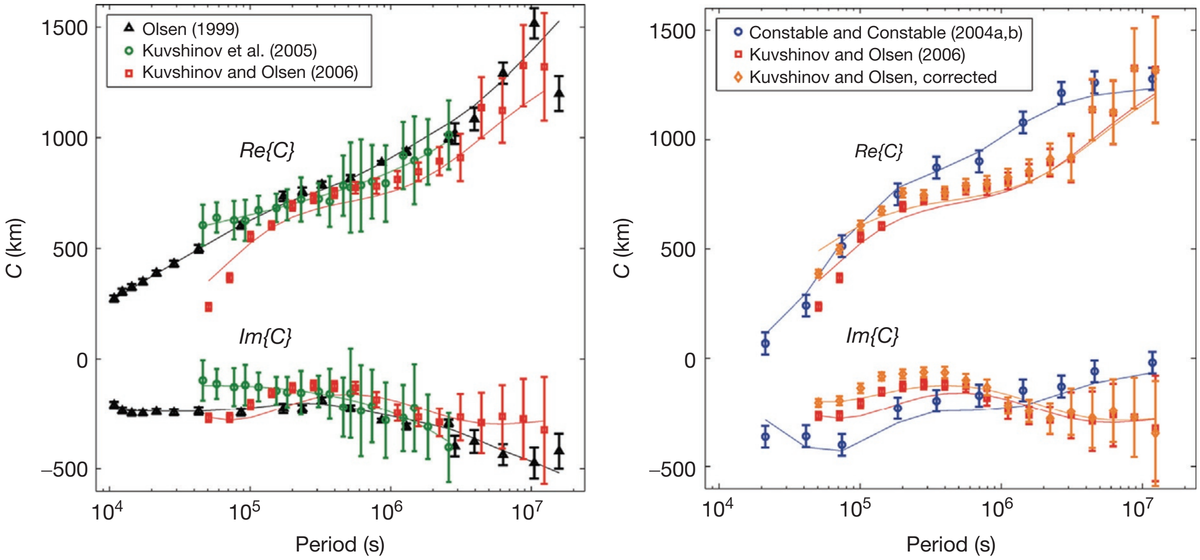

Figure 11 Long-period geomagnetic response functions computed from magnetic satellite records. Kuvshinov and Olsen (2006) attributed the difference in the long-period imaginary response between their data and those of Constable and Constable (2004b) as an artifact of Constables' time-series analysis. Their correction removes the 3D effects of the oceans on the 1D response functions. Modified from Kuvshinov A and Olsen N (2006) A global model of mantle conductivity derived from 5 years of CHAMP, Orsted, and SAC-C magnetic data. *Geophysical Research Letters* 33: L18301.

class of methods that will automatically estimate the value of these parameters (see, e.g., Gill et al., 1981). In electric and electromagnetic methods, the problems are almost always nonlinear, so fully nonlinear or linearized approaches need to be chosen.

5.07.3.3 Regularized Inversion

If one does not have an a priori justification for parameterizing the subsurface conductivity model, or such a parameterization is impractical, then some other constraint on the model space must be imposed to make the problem well posed. A popular, effective, and useful approach is to generate smooth models using some sort of regularization (see, e.g., Constable et al., 1987).

5.07.3.4 Analytic Least Squares Solutions

A true least squares solution for a given model dimensionality is a rare thing; usually, either the forward models must be trivially simple, or the nonlinear forward solution must be recast as a linear functional. Such a solution exists for the 1D resistivity-sounding problem (Parker, 1984) and for the 1D MT problem (Parker and Whaler, 1981).

5.07.3.5 MT over a Layered Earth

The simplest extension of the half-space apparent resistivity is a horizontally layered Earth. For an N-layered structure numbered downward, we can define a complex wave number for each layer

$$k_j = \sqrt{i\omega\mu_o\sigma_j} \quad i = 1, \ldots, N$$

with layer impedance

$$G_i = \frac{\mu_o\omega}{k_i}$$

Then, the total impedance of the layers $i,\ldots,N$ is given by Z_i and defined for the top of each layer by

$$Z_i = G_i \frac{Z_{i+1} + G_i \tanh(ik_i h_i)}{G_i + Z_{i+1} \tanh(ik_i h_i)}$$

where h_i are the layer thicknesses (Schmucker, 1970). Thus, Z_1 is the impedance observed at the surface and is easily computed using a recurrence relationship starting with $G_N = Z_N$.

5.07.3.5.1 *Weidelt's transformation*

An analytic solution exists for a layered, spherically symmetrical Earth conductivity model (Srivastava, 1966; see also Parkinson, 1983, p. 313). However, given the greater simplicity of the layered MT solution (in the preceding text) and the various inverse solutions available for the flat-Earth approximation (in the succeeding text), it is often desirable to analyze global data using flat-Earth solutions. Weidelt (1972) provided a compact transformation between the two geometries. If we interpret a GDS c-response $c(\omega)$ obtained for spherical harmonic degree n using a layered model to get a conductivity-depth relationship $\bar{\sigma}(z)$, this can be transformed into a conductivity profile in a spherical Earth $\sigma(r)$ of radius R using

$$\sigma(r) = f^{-4}(r/R)\bar{\sigma}\left(R\frac{(r/R)^{-n} - (r/R)^{n+1}}{(2n+1)f(r/R)}\right)$$

where

$$f(r/R) = \frac{(n+1)(r/R)^{-n} + n(r/R)^{n+1}}{2n+1}$$

which for $n=1$ reduces to

$$\sigma(r) = f^{-4}(r/R)\bar{\sigma}\left(R\frac{(R/r) - (r/R)^2}{3f(r/R)}\right)$$

and

$$f(r/R) = \frac{2R/r + (r/R)^2}{3}$$

We see from Figure 12 that the correction is only significant below depths of about 2000 km or, for typical mantle resistivities, periods of about 1 day or longer.

5.07.3.6 Forward Modeling in Higher Dimensions

Once the realm of 1D or radially symmetrical models is left, analytic solutions are no longer available for general conductivity structure, and one is forced to solve the electromagnetic governing equations numerically. For interpretation of MT data on a local scale, a 2D model is useful, especially if the data are collected along a single profile (as is often the case), and avoids the complexity of model construction and computation in three dimensions. However, for global induction problems, we are forced to take the step from 1D directly to 3D. A review of 3D modeling is provided by Avdeev (2005).

Rewriting Maxwell's equations for frequency ω and considering an applied source of current $\mathbf{J}'$ or magnetic field $\mathbf{H}'$, we have

$$\begin{aligned} \nabla \times \mathbf{E} &= -i\omega\mu(\mathbf{H} + \mathbf{H}') \\ \nabla \times \mathbf{H} &= \sigma\mathbf{E} + \mathbf{J}' \end{aligned}$$

which can be solved if the differential operators are approximated numerically. The most straightforward approach is the finite difference scheme in which $\mathbf{E}$ and $\mathbf{H}$ are discretized over a rectilinear grid of nodes, resulting in a linear system of equations $\mathbf{A}x = b$ where b represents the boundary conditions and applied source fields, x is the vector of field values on the nodes, and $\mathbf{A}$ is a matrix of difference operators. $\mathbf{A}$ is large, but sparse, making the inversion of the matrix tractable for even large problems if appropriate sparse matrix solutions are used. Alternatively, one can use algorithms that do not require the storage of the entire matrix $\mathbf{A}$ (e.g., Weiss, 2001).

A disadvantage of the finite difference approach is that the grid of nodes must be uniformly rectilinear, making it difficult to mesh complex surfaces or structure having a large range of length scales. A solution to this is the finite element approach, in which $\mathbf{E}$ and $\mathbf{H}$ are defined on the edges of triangular (2D) or tetrahedral (3D) elements and interpolated across the elements using basis functions. A linear system of equations again results in a sparse matrix to be solved. Model construction is perhaps

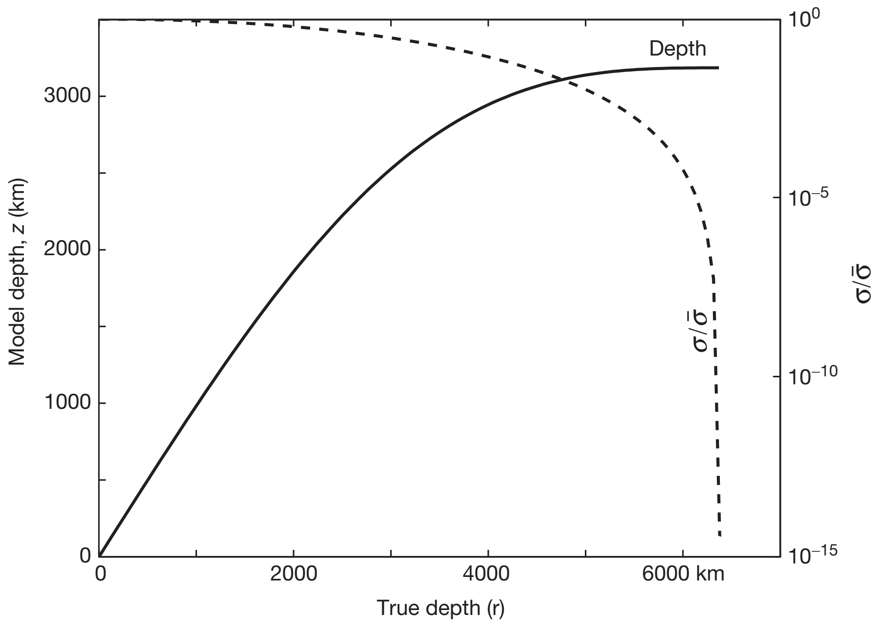

Figure 12 Weidelt's transformation for depth and conductivity, for a P_1^0 source-field geometry.

more difficult using finite elements, but automated meshing schemes are becoming available (e.g., Key and Weiss, 2006).

Usually, the equations are solved for **E** and then a discrete approximation to Faraday's law is used to recover **H**. A common approach to numerical modeling of electromagnetic fields is to break the problem into primary ($\mathbf{E}_0$, $\mathbf{H}_0$, and σ_0) and secondary ($\mathbf{E}_s$, $\mathbf{H}_s$, and σ_s) components:

$$\mathbf{E} = \mathbf{E}_0 + \mathbf{E}_s, \qquad \mathbf{H} = \mathbf{H}_0 + \mathbf{H}_s, \qquad \sigma = \sigma_0 + \sigma_s$$

where the primary fields have an analytic solution, such as a whole-space, half-space, or layered model. This primary/secondary separation not only has many advantages, particularly if there is a singularity associated with a man-made source field, but also provides the basis for the third approach to high-dimensional modeling, the integral equation method. If the region over which σ_s is nonzero is a finite volume V, then

$$\mathbf{E}_s = \int_V \mathbf{G}^{\mathrm{E}}(\mathbf{r}, \mathbf{r}')\sigma_s \mathbf{E}(\mathbf{r}')\, \mathrm{d}v'$$

and

$$\mathbf{H}_s = \int_V \mathbf{G}^{\mathrm{H}}(\mathbf{r}, \mathbf{r}')\sigma_s \mathbf{E}(\mathbf{r}')\, \mathrm{d}v'$$

where **G** are the 3 × 3 tensor Green's functions relating the fields at **r** to current elements at **r**′. The discretization of these equations leads to a linear system where **A** is now dense, but much smaller than for the finite element and finite difference methods. All of these approaches can be projected onto spherical geometries in order to model global electromagnetic induction (e.g., Everett and Schultz, 1996; Grammatica and Tarits, 2002; Kuvshinov et al., 2002; Martinec, 1999; Uyeshima and Schultz, 2000; Weiss and Everett, 1998; Yoshimura and Oshiman, 2002).

A frequency domain approach, which assumes a stationary excitation of the source field at a given frequency ω, may not be appropriate if one wants to consider the effect of a discrete magnetic storm. In this case, a time-domain approach to modeling is required (Hamano, 2002; Kuvshinov and Olsen, 2004; Velimsky et al., 2003).

5.07.3.7 Numerical Inversion of Geomagnetic Data

The first thing one needs for an inversion scheme is a measure of how well a given model fits the data. For practical and theoretical reasons, the sum-squared misfit is favored:

$$\chi^2 = \sum_{i=1}^{M} \frac{1}{\sigma_i^2}[d_i - f(x_i, \mathbf{m})]^2$$

where

$$\mathbf{d} = (d_1, d_2, d_3 \ldots, d_M)$$

are M observed data values,

$$\mathbf{x} = (x_1, x_2, x_3 \ldots, x_M)$$

are independent data variables (electrode spacing, frequency, etc.), and

$$\mathbf{m} = (m_1, m_2 \ldots, m_N)$$

are model parameters (layer or block conductivities, layer or block sizes, etc.). Equivalently, the misfit may be written as

$$\chi^2 = \left\| \mathbf{W}\mathbf{d} - \mathbf{w}\widehat{\mathbf{d}} \right\|^2$$

where $\widehat{\mathbf{d}}$ is the predicted response from the model

$$\widehat{\mathbf{d}} = f(\mathbf{x}, \mathbf{m})$$

and **W** is a diagonal matrix of reciprocal data errors

$$\mathbf{W} = \mathrm{diag}(1/\sigma_1, 1/\sigma_2, \ldots, 1/\sigma_M)$$

The least squares approach attempts to minimize χ^2 with respect to all the model parameters simultaneously. If the data errors σ_i are Gaussian and independent, then least squares provides a maximum likelihood and unbiased estimate of $\mathbf{m}$, and χ^2 is chi-square distributed with $M-N$ degrees of freedom. To apply linear inverse theory to nonlinear electromagnetic data, we need to linearize the problem by expanding f around an initial model guess $\mathbf{m}_0$

$$\widehat{\mathbf{d}} = f(\mathbf{m}_1) = f(\mathbf{m}_0 + \Delta\mathbf{m}) \approx f(\mathbf{m}_0) + \mathbf{J}\Delta\mathbf{m}$$

where $\mathbf{J}$ is a matrix of derivatives of data with respect to the model

$$J_{ij} = \frac{\partial f(x_i, \mathbf{m}_0)}{\partial m_j}$$

(often called the Jacobian matrix) and

$$\Delta\mathbf{m} = (\delta m_1, \delta m_2, \ldots, \delta m_N)$$

is a model parameter perturbation about $\mathbf{m}_0$. Now, our expression for χ^2 is

$$\chi^2 \approx \|\mathbf{Wd} - \mathbf{W}f(\mathbf{m}_0) + \mathbf{WJ}\Delta\mathbf{m}\|^2$$

which we minimize in the usual way by setting the derivatives of χ^2 with respect to $\Delta\mathbf{m}$ equal to zero to get N simultaneous equations:

$$\beta = \alpha\Delta\mathbf{m}$$

where

$$\beta = (\mathbf{WJ})^{\mathrm{T}}\mathbf{W}(\mathbf{d} - f(\mathbf{m}_0))$$
$$\alpha = (\mathbf{WJ})^{\mathrm{T}}\mathbf{WJ}.$$

The matrix α is sometimes called the curvature matrix. This system can be solved for $\Delta\mathbf{m}$ by inverting α numerically, and a second model $\mathbf{m}_1 = \mathbf{m}_0 + \Delta\mathbf{m}$ found. Because $\mathbf{J}$ depends on $\mathbf{m}$, one needs to solve this repeatedly and hope for convergence to a solution. Near the least squares solution, this method will work, but any significant nonlinearity will result in likely failure. An algorithm to compensate for this behavior was suggested by Marquardt (1963). The diagonal terms of the curvature matrix are increased by a factor λ:

$$\begin{aligned} \alpha_{jk} &= \alpha_{jk}(1+\lambda) \qquad && \text{for } j = k \\ \alpha_{jk} &= \alpha_{jk} && \text{for } j \neq k \end{aligned}$$

For small λ, this method obviously reduces to the linearized inversion. For large λ, the diagonal terms dominate and the method reduces to a gradient algorithm that chooses a path in the direction of maximum reduction in χ^2 (the method of steepest descent). The gradient algorithm is robust to nonlinearity but is very inefficient in the parabolic region near the solution (because the gradient gets small; ultimately zero). By adjusting λ to be large far from the solution and small as we approach the minimum, we have a fairly stable method of determining a model composed of a small number of parameters.

For nonlinear problems that are truly parameterized (e.g., finding the concentration and mobility of a charge carrier in a mineral), the Marquardt method is pretty hard to beat. It also works fairly well for problems where the number of degrees of freedom is large, given by $M-N$ when the M data are truly independent, and the starting model provides a rough fit to the data. In practice, this means that 1D models consist of a small number of layers. Any attempt to increase the number of layers significantly, to approximate the realistic case of a continuously varying conductivity, or to invert a 2D or 3D model with thousands or millions of parameters will result in wildly fluctuating parameters followed by failure of the algorithm. This is because there will be columns of $\mathbf{J}$ that are small, reflecting the fact that large variations in a model parameter may relate to negligible effects on the combined data.

One approach, suggested by Backus and Gilbert (1967), is to minimize $\Delta\mathbf{m}$, but this and related algorithms converge extremely slowly and are called by Parker (1994) 'creeping methods.' In any case, the true least squares solutions can be pathologically rough – for the 1D MT case, it is known that the least squares solution is composed of delta functions in conductivity. Almost all high-dimensional inversion today incorporates some type of regularization, an approach suggested by Tikhonov and Arsenin (1977), which explicitly penalizes bad behavior in the model. For example, instead of minimizing χ^2, we minimize an unconstrained functional

$$U = \|\mathbf{Rm}_1\|^2 + \mu^{-1}\left(\|\mathbf{Wd} - \mathbf{W}f(\mathbf{m}_1)\|^2 - \chi_*^2\right)$$

where χ_*^2 is a target misfit that is greater than the minimum possible, but statistically acceptable, and $\mathbf{Rm}$ is some measure of roughness in the model, often taken to be first differences between adjacent model parameters and easily generated by a matrix $\mathbf{R}$ consisting of $(-1, 1)$ entries on the diagonal. Minimizing U has the effect of minimizing model roughness and how far the data misfit is from being acceptable. We substitute our linearization around $f(\mathbf{m}_0)$ and differentiate U with respect to $\mathbf{m}_1$ to accomplish this, rearranging the result to get $\mathbf{m}_1$ directly:

$$\mathbf{m}_1 = \left(\mu\mathbf{R}^{\mathrm{T}}\mathbf{R} + (\mathbf{WJ})^{\mathrm{T}}\mathbf{WJ}\right)^{-1}(\mathbf{WJ})^{\mathrm{T}}\mathbf{W}(\mathbf{d} - f(\mathbf{m}_0) + \mathbf{Jm}_0)$$

We need only to choose the trade-off (Lagrange) multiplier μ. The approach of Constable et al. (1987) was to note that for each iteration χ^2 is a function of μ and to use 1D optimization (simply a line search) to minimize χ^2 when $\chi^2 > \chi_*^2$ and to find μ such that $\chi^2 = \chi_*^2$ otherwise. They called this approach 'Occam inversion.' Although the Occam algorithm is reliable and has good convergence behavior, the computation and storage of $\mathbf{J}$ for large models can be limiting, and numerous other regularization approaches using conjugate gradient algorithms and approximate derivatives exist (e.g., Mackie and Madden, 1993; Newman and Alumbaugh, 2000; Smith and Booker, 1991).

5.07.3.8 Analytic Inversion and Estimation of Bounds

The 1D MT problem is one of the few problems for which an analytic least squares solution exists. Parker and Whaler (1981) (see also Parker, 1994) showed that the c-response (also called admittance by Parker, since the electric field is a response to the forcing magnetic field) can be cast as a linear functional of a spectral function that is in turn nonlinearly related to conductivity. Linear inverse theory can be used to find a least squares solution for a given data set in terms of the spectral function, which can then be used to recover a conductivity distribution. The math is nontrivial, and interested readers are referred to the original works, but the result is that least squares solutions to the 1D MT problem are delta functions of conductivity in an infinitely resistive half-space, a model space called D^+ by Parker. This is one of the reasons why layered least squares solutions are not stable as the layer number increases past the point of restricting variations in conductivity to be few and far between. It may appear that such a pathological solution is not useful, but being able to put a lower bound on the possible 1D misfit is very useful when choosing desired misfits for regularized inversions, and the inversion machinery of D^+ also allows the estimation of a maximum depth of resolution available for a given data set. Also, the algorithm can be used to test the compatibility of resistivity and phase data and put bounds on missing data (Parker and Booker, 1996).

Another approach to interpreting response function data is to put bounds on average conductivity over a given region of the Earth. The earliest attempt at this by Backus and Gilbert (1968) suffers from being a linearized theory; this may not be too much of a restriction for seismology, but in geomagnetic induction, the range of possible conductivities is so large as to make this approach essentially useless. A nonlinear approach using electromagnetic data was first presented via the funnel functions of Oldenburg (1983). More recently, Medin et al. (2006) generalized this by using quadratic programming to solve for electric conductivity and the forward responses simultaneously, by making both the data and the forward solution equations constraints in the optimization. The flexibility of the optimization approach allows many other constraints, such as monotonicity of conductivity with depth and bounds on average conductivity, to be applied. By systematically solving for various averages of conductivity over depth, the bounds of acceptable averages can be discovered.

To date, attempts to put bounds on average conductivity have been restricted to the 1D problem. One might try to extend the machinery to higher dimensions, but bounded solutions to the 2D MT problem may not exist (Robert Parker, personal communication, 2013).

5.07.4 Electric Conductivity of Earth Materials

There are three basic conduction regimes for crustal and mantle rocks:

(1) *Ionic conduction* of crustal rocks containing water. The mineral grains making up most rock-forming minerals are essentially insulators (e.g., quartz's conductivity at surface temperatures is about 10^{-12} S m^{-1}), and so the higher conductivity of water in pores and cracks determines the conductivity of the rock.

(2) Conduction dominated by minerals that are *good semiconductors* or *metals*, such as graphite, magnetite, and pyrite, or native metals. These minerals may occur in trace amounts that nevertheless form a well-connected pathway, or in extreme cases, they may account for the bulk of the rock, in the case of ore bodies.

(3) *Thermally activated conduction* in subsolidus or molten silicates at elevated temperature, either in the deep mantle or crustal volcanic systems (Table 2).

Table 2 Approximate conductivities and resistivities of various Earth materials

Ionic conduction through water		
Seawater at 20 °C	5 S m^{-1}	0.2 Ω m
Seawater at 0 °C	3 S m^{-1}	0.3 Ω m
Marine sediments	1–0.1 S m^{-1}	1–10 Ω m
Land sediments	0.001–0.1 S m^{-1}	10–1000 Ω m
Igneous rocks	10^{-5}–10^{-2} S m^{-1}	100–100 000 Ω m
Good semiconductors		
Graphite	10 000–1 000 000 S m^{-1}	10^{-4}–10^{-6} Ω m
Galena	10–100 000 S m^{-1}	10^{-1}–10^{-5} Ω m
Pyrite	1–1000 S m^{-1}	10^{-3}–1 Ω m
Magnetite	20 000 S m^{-1}	5×10^{-5} Ω m
Thermally activated conduction		
Olivine at 1000 °C	0.0001 S m^{-1}	10 000 Ω m
Olivine at 1400 °C	0.01 S m^{-1}	100 Ω m
Tholeiite melt	3 S m^{-1}	0.3 Ω m
Silicate perovskite	1 S m^{-1}	1 Ω m

5.07.4.1 Moving an Electric Charge

Electric conduction in a material is accomplished by a movement of charge, which in practice means the movement of electrons, holes (the absence of an electron), ions, or ion vacancies. Materials may be classified on the basis of the nature of the charge carriers and the type of movement. Generally, conductivity in a material is given by

$$\sigma = nq\mu$$

where q is the charge of the mobile species, n is the concentration of the charged species, and μ is the mobility or drift velocity per applied electric field, $|v/E|$.

5.07.4.1.1 Conduction in native metals

Conduction in native metals is by means of valence, or conduction, electrons that do not take part in crystal bonding and are loosely bound to atoms. This form of conduction is very efficient, resulting in room temperature conductivities for metals of about 10^7 S m^{-1}. The conductivity of metals decreases with increasing temperature because of thermal agitation of the conduction electrons, which impedes their movement in response to an electric field and therefore lowers the drift velocity. Native metals are fairly rare in surface rocks, but metallic iron is responsible for high conductivity in the core.

Metallic conduction electrons have long mean free paths because they do not get deflected by the periodic arrangement of ion cores and only rarely get scattered off other conduction electrons. For metals,

$$v = \frac{-eE\tau}{m}$$

where τ is the mean free time between collisions and m is the mass of the electron. For metals, n is of order 10^{28}–10^{29} m^{-3}. The mean free path ($v\tau$) is of order 1 cm at 4 K, 10^{-8} m at room temperature. Thus, conductivity from metals is thus given by

$$\sigma = \frac{ne^2\tau}{m}$$

This can be thought of as an acceleration under an electric field (e/m) of charge of density ne for a time period τ.

Scattering (which determines mobility μ and mean free time τ) is by means of phonons (lattice vibrations) and impurities. Phonons go to zero at 0 K and are proportional to temperature above some threshold, so

$$\rho \propto T$$

(That threshold is the Debye temperature, below which quantization of energy causes some vibration modes to be 'frozen' out. It is between 100 and 400 K for most metals.)

5.07.4.1.2 Semiconduction

Semiconduction is the result of behavior in between metallic conduction and conduction in insulators. It is typical of ionically bonded binary compounds, such as PbS, ZnS, and MgO. There are no free electrons, as such, in a semiconductor, but an applied electric field can supply enough energy to move electrons from the valence band, across the band gap E_g, into the conduction band at higher energy levels. As a result of these few electrons and the holes they leave behind in the lower energy levels, moderate conductivities are achieved, between about 10^{-5} and $10^{5}\ \mathrm{S\,m^{-1}}$. Sulfide minerals are often semiconductors with quite low resistivities.

For semiconductors,

$$\sigma = ne\mu_e + pe\mu_h$$

where n and p are the carrier densities of electrons and holes (typically around 10^{19}–$10^{23}\ \mathrm{m^{-3}}$) and μ_e and μ_h are the respective mobilities. Carrier concentration is thermally activated and is

$$n \propto T^{3/2} \mathrm{e}^{-E_g/2kT}$$

where k is the Boltzmann constant ($1.380 \times 10^{-23}\ \mathrm{J\,K^{-1}}$ or 8.617×10^{-5} eV). Mobility is also only proportional to T, so the exponential term dominates. Such thermally activated processes are often termed Arrhenius relationships and produce linear plots when $\log(\sigma)$ is plotted against $1/T$.

Charge carriers can also be generated by impurities or doping; for example, a divalent cation substituting on a trivalent site will have an excess electron that is available for the conduction band. These two conduction regimes, one determined by statistical mechanics and one determined by crystal impurities, are typical of solid-state conduction. The first, purely thermally activated, variation in conductivity is the same for a given material and temperature and is called 'intrinsic' conduction. The second regime, which also has some temperature dependence but will vary from sample to sample with the amount of impurity, is called 'extrinsic' conduction. In the intrinsic regime, holes must equal electrons because the elevation of every electron into the conduction band will leave behind a hole. Impurities, however, can donate either holes or electrons to conduction (Figure 13).

5.07.4.1.3 Ionic, or point defect, conduction

Conduction by point defects dominates when the band gap is too large for semiconduction and is the result of moving ions and ion vacancies through a crystal structure. It is very difficult to move ionically bonded ions through a crystal lattice, so the resistivities of silicate minerals are very high; quartz has resistivities between 10^{10} and $10^{14}\ \Omega$ m and rock salt has a resistivity of $10^{12}\ \Omega$ m or so. It would, in fact, be close to impossible to move ions through a perfect lattice, but defects in the lattice allow the motion of ions and vacancies. Schottky defects are lattice vacancies and Frenkel defects are ions in interstitial positions. Impurities also constitute defects in the lattice, both in themselves and because they can promote vacancies to maintain charge balance. These are called point defects, compared with dislocations, line, and plane defects, which tend not to contribute substantially to conduction (Figure 14).

Schottky and Frenkel defects are thermally induced, so the number of defects, and hence conductivity, increases with increasing temperature:

$$n_s = N\,\mathrm{e}^{-E_v/kT}$$

(Schottky defects or vacancies)

$$n_f = (NN')^{1/2} \mathrm{e}^{-E_i/2kT}$$

(Frenkel defects or interstitials) where N is the total number of atoms and N' is the total number of interstitial sites. Again, however, defects can be generated by impurities. Thus, a divalent cation on a monovalent site induces a cation vacancy to maintain charge neutrality.

The mobility of point defects can be related to diffusion, the flux $\mathbf{J}_N$ of atoms crossing unit area in unit time under the

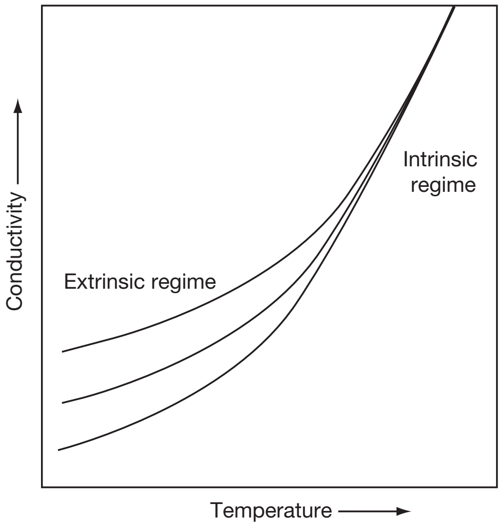

Figure 13 Extrinsic and intrinsic regimes in semiconductors. Extrinsic conduction occurs at lower temperature and is a result of electrons or holes generated by impurities (or doping). Intrinsic conduction is a result only of thermally activated charge carriers associated with the pure crystal.

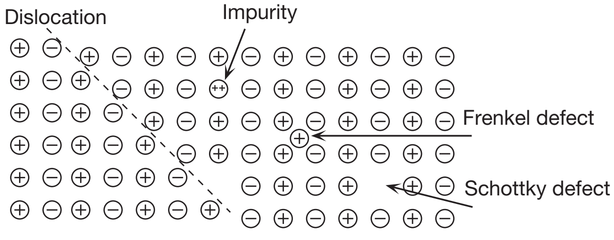

Figure 14 Defects in crystals.

influence of a concentration gradient ∇N. The diffusivity, or diffusion constant, D is defined by *Fick's law*:

$$\mathbf{J}_N = -D\nabla N$$

Diffusivities are found to vary with temperature, again as a thermally activated Boltzmann process:

$$D = D_\mathrm{o}\mathrm{e}^{-E_\mathrm{d}/kT}$$

where E_d is another activation energy for diffusivity.

Mobilities are related to diffusivities by the Nernst–Einstein equation

$$kT\mu = qD$$

so $\mu = qD/kT$ and the conductivity of, for example, Schottky defects becomes

$$\begin{aligned}\sigma &= n_\mathrm{s}q\mu \\ &= N\mathrm{e}^{-E_v/kT}qqD/kT \\ &= Nq^2D_\mathrm{o}/kT\mathrm{e}^{-E_v/kT}\mathrm{e}^{-E_\mathrm{d}/kT}\end{aligned}$$

(much of the earlier-mentioned material can be found in Kittel, 1986). The exponential terms dominate, and so to a first approximation, conductivity is given by

$$\sigma = \sigma_\mathrm{o}\mathrm{e}^{-E/kT}$$

where E is an apparent activation energy associated with both defect concentration and mobility. Often, there are several point defects in the mineral; **Figure 15** presents a model of 11 different charge-carrying defects in silicate perovskite, and olivine would have a similar suite of defects. The description of the defects is handled by the Kröger–Vink notation, in which the main character is the actual species involved (a 'V' denotes a vacancy), the subscript is the crystal site for a normal lattice (in interstitial site is denoted by 'I'), and the superscript is negative, positive, or neutral charge shown as ′, •, or x, respectively. Thus, $\mathrm{Fe}^{\bullet}_{\mathrm{Mg}}$ is a Fe^{3+} ion occupying a Mg^{2+} site resulting in a net charge for the defect of $+e$.

In spite of the variety in defect types, the dominance of the exponential term in the expression for conductivity means that at a given temperature, one mechanism is likely to dominate over another. As temperature changes, different activation energies will cause the dominant conduction mechanism to change, so conductivity is often expressed as

$$\sigma = \sum_i \sigma_i \mathrm{e}^{-E_i/kT}$$

The Boltzmann relationship between temperature and conductivity can be linearized by taking $\log(\sigma)$ as a function of $1/T$, to form an Arrhenius plot. For a single conduction mechanism, data plotted in this way will be a straight line. For mixed conduction, a number of lines may be observed as a function of temperature. **Figure 16** shows an example of two conductivity mechanisms being expressed as a sample is heated from 500 to 1200 °C.

5.07.4.1.4 Pressure

Pressure can also have an effect on conductivity, which may be modeled as

$$\sigma = \sigma_\mathrm{o}\mathrm{e}^{-(E+p\Delta V)/kT}$$

where P is pressure and ΔV is called the activation volume. Pressure usually has a minor effect compared with temperature, unless it changes the mineral phase and causes a more mobile or numerous defect to dominate.

One of the biggest effects on defect chemistry is oxygen. Oxidation and reduction are associated with an exchange of charge, so oxidation state changes the number of charged defects in a mineral. The model for perovskite in **Figure 15**

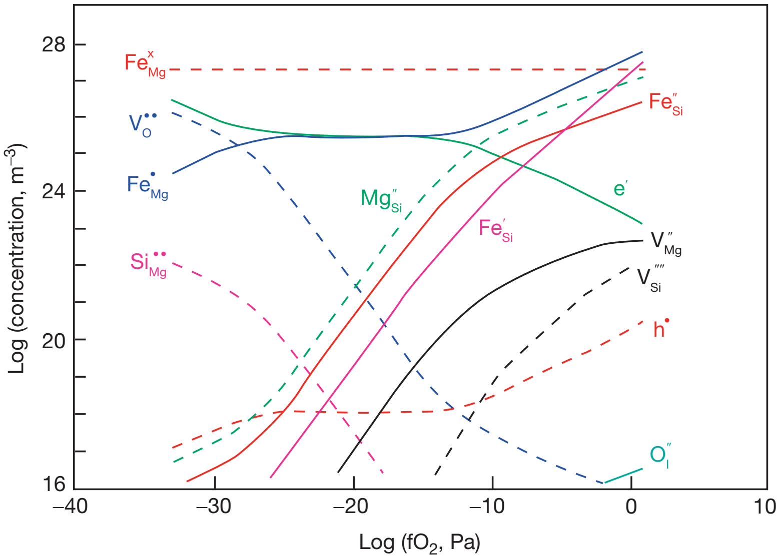

Figure 15 A defect model for silicate perovskite, showing concentrations of various defects as a function of oxygen activity ($f\mathrm{O}_2$). Modeled temperature is 2500 K (2227 °C) and pressure is 40 GPa. Redrawn from Hirsch LM and Shankland TJ (1991) Point defects in (Mg, Fe)SiO_3 perovskite. *Geophysical Research Letters* 18: 1305–1308.

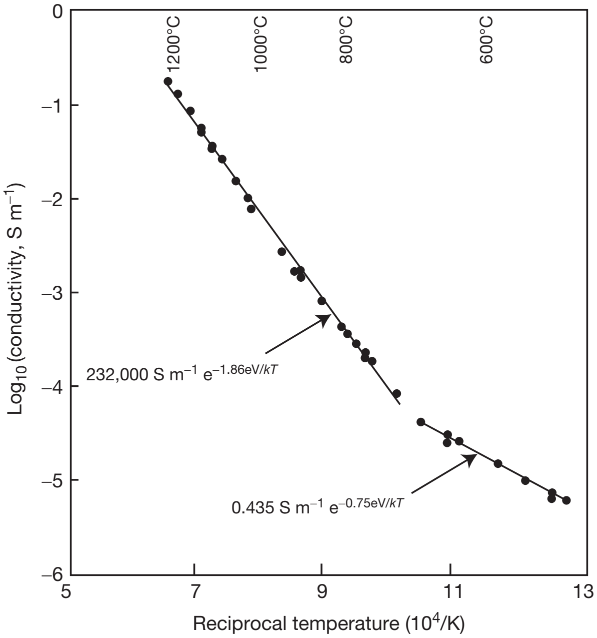

Figure 16 Electric conductivity data for cobalt olivine (Co_2SiO_4), showing two conduction mechanisms expressed as Arrhenius relationships of two different activation energies. Redrawn from Hirsch LM (1990) Electrical conduction in Co_2SiO_4. *Physics and Chemistry of Minerals* 17: 187–190.

gives some idea of how defects in a mantle mineral depend greatly on oxidation state.

5.07.4.1.5 *Aqueous electrolytic conduction*

Aqueous conduction is associated with ions dissociated in water and is arguably the most important conduction mechanism in crustal rocks. The dominant dissolved salt is sodium chloride, and it is clear that the number of charge carriers depends simply on the concentration of salt. Mobility increases with temperature because the viscosity of water decreases with temperature, and for seawater concentration (32 g l^{-1}), conductivity is approximately

$$\sigma = 3 + T/10\,\mathrm{S\,m^{-1}}$$

for temperature T in Celsius. However, for water under pressure, this linear relationship breaks down at around 200 °C, and saltwater conductivity peaks at between 300 and 400 °C (Quist and Marshall, 1968).

5.07.4.1.6 *Clay minerals*

Clays have an important effect on aqueous conduction in crustal rocks, because they have a surface charge, usually negative, associated with their crystal structure. This creates a so-called 'double layer' of charge, the negative charge on the crystal creating a diffuse layer of positive charge in the electrolyte that is mobile and can contribute to electric conduction. This effect is greatest for low-salinity groundwater and, in practice, limits the effective resistivity of pore water. A good description of this surface electrochemistry is found in Morgan et al. (1989) and a comprehensive treatment of surface conductance by Revil and Glover (1997).

5.07.4.1.7 *Magma*

Magma conductivity is approximately that of seawater and is associated with diffusion of ions in a highly polymerized structure. So, it is not surprising that again, one observes a thermally activated Boltzmann-type conductivity, which for tholeiitic melt above 10 kbar pressure is approximately (Tyburczy and Waff, 1983)

$$\sigma = 10^{5.332}\mathrm{e}^{-1.533\,\mathrm{eV}/kT}$$

How well a mixture of melt and rock conducts electricity depends on melt fraction, temperature, composition, and the geometry of the partial melt (Roberts and Tyburczy, 1999). The relationship between geometry and conductivity of two-component systems is discussed in the next section.

5.07.4.2 Binary Mixing Laws

We have seen that rocks are often made up of two components, one very much more conductive than the other. For example, a gabbro could be mostly nonconducting silicate minerals with minor amounts of conductive magnetite. A sandstone can be nonconducting quartz saturated with water.

A mantle rock can be subsolidus silicates of several hundred ohmmeters with conductive melt between the grains. Rather than make measurements on every possible combination, binary mixing laws can be used to predict the conductivity of the bulk rock as a function of the conductive fraction. As one might imagine, the physical geometry of the conductive material very much determines how conductive the bulk rock ends up.

The classic binary mixing relationship is Archie's law, which (in spite of the name) is an entirely empirical relationship developed to explain the conductivity of sedimentary rocks containing water:

$$\sigma = \sigma_\mathrm{s} + (\sigma_\mathrm{f} - \sigma_\mathrm{s})\beta^\mathrm{m}$$

Here, σ_f is the fluid, or water conductivity, and β is the fluid fraction. In the case of a saturated rock, β is the porosity, but it is easy enough to express fluid content in terms of saturation and porosity. Here, we have included the conductivity of the solid, σ_s, although for silicate minerals at crustal temperatures, this is usually taken to be zero. The exponent m can be derived experimentally from a suite of samples for a given rock type but is usually taken to be 2 for sediments. A smaller m corresponds to more efficiently connected pore space.

A model of fluid-filled tubes might be a reasonable representation of well-connected melt in a volcanic system:

$$\sigma = \frac{1}{3}\beta\sigma_\mathrm{f} + (1-\beta)\sigma_\mathrm{s}$$

Models for binary systems can become quite complicated; various geometries are presented by Schmeling (1986). However, all possible models must lie between the Hashin–Shtrikman (HS) bounds:

$$HS^- = \sigma_\mathrm{s} + \beta\left(\frac{1}{\sigma_\mathrm{f}-\sigma_\mathrm{s}} + \frac{1-\beta}{3\sigma_\mathrm{s}}\right)^{-1}$$

$$HS^+ = \sigma_\mathrm{f} + (1-\beta)\left(\frac{1}{\sigma_\mathrm{s}-\sigma_\mathrm{f}} + \frac{\beta}{3\sigma_\mathrm{f}}\right)^{-1}$$

Normally, when one measures the electric conductivity of fluid-filled crustal rocks as a function of pressure, increasing pressure decreases pore volume, and so conductivity decreases. However, if the dominant conduction is by conductive minerals, such as graphite or magnetite, increasing pressure can press these minor minerals into better electric contact, in which case conductivity will increase with pressure. This is an important diagnostic of conduction mechanism (Shankland et al., 1997).

5.07.4.3 Polarization

We have discussed various conduction mechanisms – metallic, semiconduction, ionic conduction, and electrolytic conduction – all of which can be found in rocks and minerals and within the apparatus we used to make measurements. When one attempts to pass electric current between two different types of conductors, there will be a polarization at the boundary. The classic example of this will be a metallic electrode making contact with the ground or a laboratory sample. Electrons flowing through the circuit set up an electric field in the electrolyte. Ions drift through the fluid in response to this field until they encounter the electrodes, where they have to stop. The initial effect of this is to increase the impedance of the fluid (and change the phase of the conduction current) by depleting the ions available for transport and the distance over which they can migrate. A second effect is that the ions may then participate in reversible and irreversible electrochemical reactions with the electrodes.

5.07.4.4 Anisotropy

So far, we have only considered the case in which conductivity is isotropic. In general, conductivity may depend on direction:

$$\sigma = \begin{bmatrix} \sigma_x & & \\ & \sigma_y & \\ & & \sigma_z \end{bmatrix}$$

where most commonly x, y, and z correspond to two horizontal and the vertical direction, although any general case can be rotated into three principal axes.

As with porosity, the nature of anisotropy depends on scale, which can loosely be classified as crystallographic anisotropy, textural anisotropy, and structural anisotropy as the scale length gets progressively larger.

5.07.4.4.1 Crystallographic anisotropy

Crystallographic anisotropy is associated with variations in conductivity of the mineral itself. The principal components of crystallographic properties must lie along the crystal axes, and so it is sufficient to measure and specify conductivity along these directions.

5.07.4.4.2 Textural anisotropy

Textural anisotropy is associated with the fabric of the rock. A common example of this type of anisotropy is found in sedimentary rocks that have well-developed bedding, either as a consequence of platy or tabular mineral grains that preferentially fall flat during deposition or by fine-scale interbedding. In this case, conductivity will always be higher in what were originally the subhorizontal directions (i.e., foliation direction) and lower in the direction across the beds. Anisotropy ratios (σ_y/σ_z) of up to 2–10 are possible in this way.

5.07.4.4.3 Structural anisotropy

Structural anisotropy is caused by macroscopic features that would normally be resolved by geologic mapping but that are too small in relation to the electric measurements to be resolved. For example, interbedded, meter-thick sedimentary horizons of different resistivity that are buried 10–100 m deep will appear anisotropic to a surface-based electric method but not to borehole logging.

Although in principle all three principal directions of conductivity can vary, if rocks are anisotropic, it is usually uniaxial anisotropy – that is, only one of the three directions differing from the other two. It is interesting to consider the relationship between the mathematical description and the physical interpretation of the six possibilities associated with uniaxial anisotropy, shown in Figure 17.

5.07.4.5 Laboratory Measurement of Conductivity

While the fundamental physical property of rocks and minerals is conductivity (which may be expressed as equivalent resistivity), our laboratory equipment is designed to measure circuit resistance. Resistivity ρ and resistance R for a regular prism are related by

$$R = \rho L/A$$

where L is the length of the sample and A is the cross-sectional area of the electrode-covered faces. It can be seen that if one takes a cubic meter of material ($L=1$; $A=1$), the series resistance in ohms across two opposite faces of the cube will be the same number as the resistivity in ohmmeter.

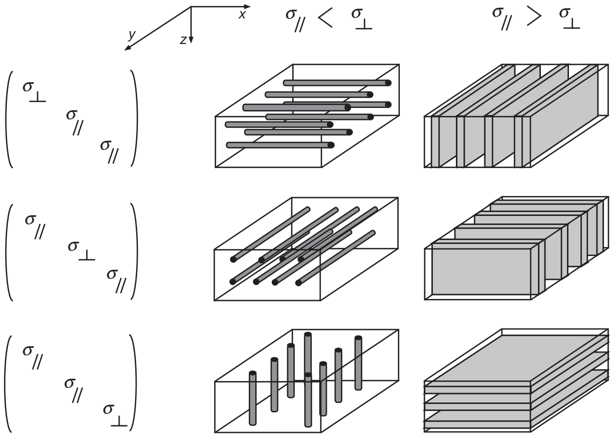

Figure 17 Relationship between geologic and mathematical descriptions of anisotropy. Here, the more conductive material is shown in gray. Rodlike conductive structure (left) corresponds to the background material ($\sigma_{//}$) being less conductive, and sheetlike conductive structure (right) corresponds to the background material being more conductive. Modified from Everett ME and Constable S (1999) Electric dipole fields over an anisotropic seafloor: Theory and application to the structure of 40 Ma Pacific Ocean lithosphere. *Geophysical Journal International* 136: 41–56.

Such a measurement can be made in practice on a regular prism (such as a rock core or mineral sample) when electric current is passed through the sample by means of two metal plates pressed to the end faces. This is called the 'two-electrode method,' but it suffers from the limitation that the contact resistance of the electrodes must be much lower than the resistance of the sample. If L is small compared with A and the sample is of relatively high ρ, this approximation is acceptable, because the contact resistance of the electrodes will be less than the resistance through the sample. Otherwise, the solution is the 'four-electrode method' (**Figure 18**). This solves the problem of contact resistance at the electrodes by measuring a potential difference across the center of the rock rather than the ends. Because modern voltmeters have very high input impedances, the contact resistance on the potential measurement circuit does not have a significant impact on the potential across the sample, and the resistivity can be computed from $\rho = \Delta VA/(I_s)$ where s is the potential electrode spacing. Practical considerations often force the issue in favor of the two-electrode method (e.g., measurements made on small samples at high temperature and pressure).

Polarization at the sample-electrode interface is controlled by using an AC current, usually of around 1 kHz. Since polarization creates a capacitive response, it is wise to measure the phase, as well as the magnitude, of the conduction current versus applied potential. A technique called impedance spectroscopy exploits this capacitive effect to examine the sample more closely, by varying the frequency of the applied voltage and monitoring both the in-phase (real) and out-of-phase (quadrature or imaginary) current. An impedance diagram is constructed, plotting imaginary versus real impedance for various frequencies (such a diagram is also called a Cole–Cole plot). An equivalent circuit of a resistor and capacitor in parallel will create a semicircular arc on such a plot (**Figure 19**). If several conduction mechanisms are present, several arcs will be generated, and in particular, electrode contact impedance in two-electrode measurements will separate from the impedance of the sample. Grain surface impedance can also be separated from grain-interior impedance this way (e.g., Tyburczy and Roberts, 1990; **Figure 20**).

When measurements are made at high temperature to predict the behavior in the deep Earth and to establish an activation energy for the conducting species, care must be taken to control the chemical environment of the sample so that it is not altered during measurement and that the conditions are applicable to the natural environment of the sample. The most obvious problem is oxidation during heating; even laboratory-grade inert gases have enough contaminant oxygen to place some minerals outside their stability fields.

For low-pressure experiments, a controlled mixture of CO:CO_2 or H:CO_2 is passed over the sample. For a given temperature and gas mix ratio, there is a known equilibrium concentration of oxygen developed; any excess is consumed by the reducing agent (CO or H), and any deficiency is liberated by the oxidizing agent (CO_2). For example,

$$2CO + O_2 \rightleftharpoons 2CO_2$$

so even if the starting gases contained contaminant oxygen, it will be consumed until only the equilibrium amount remains. Other problems associated with the chemical state of the sample are iron loss to platinum electrodes and migration of chemical species such as silicon between constituents of a multiphase sample.

Since the two-electrode method is usually used for relatively resistive samples, and often at high pressure, care has to be taken to ensure that the dominant conduction path is through the sample and not through the sample holder and surrounding apparatus. **Figure 21** shows an example of a furnace

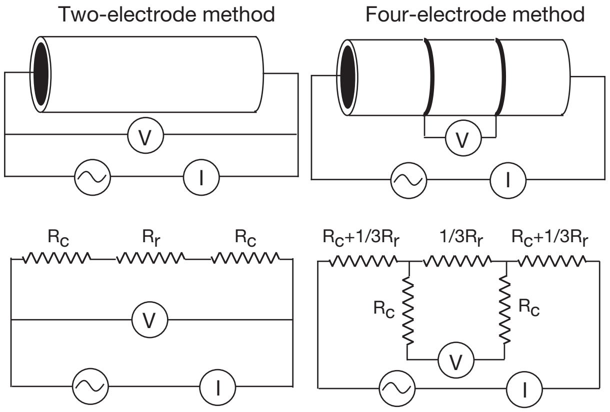

Figure 18 Two- and four-electrode methods of measuring rock resistivity, showing equivalent circuit elements. R_c is the contact or electrode resistance; R_r is the rock or sample resistance. In the two-electrode method, the potential drop across the current electrodes is measured along with the potential drop across the sample. In the four-electrode method, the potential drop across the current electrodes is not part of the voltage measuring circuit, and the potential electrode impedance simply adds to the already high input impedance of the voltmeter.

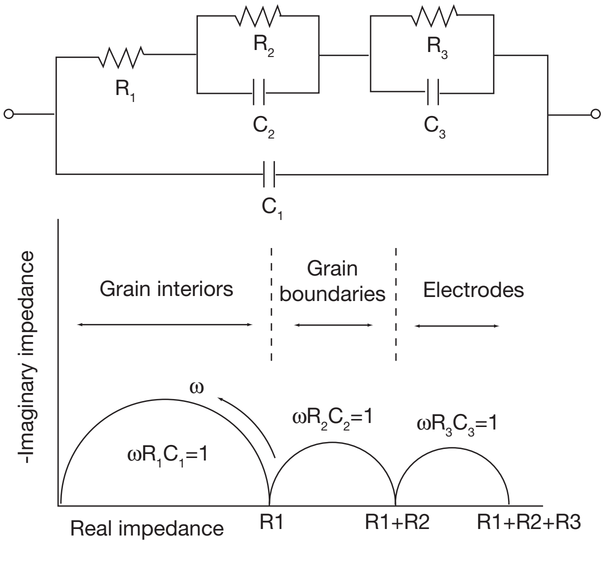

Figure 19 Impedance spectroscopy can identify the different series of conduction paths in the sample because they can be associated with different capacitive effects. The top diagram shows an equivalent series circuit, and the lower diagram shows the ideal measurement that would be made on a rock sample. Frequency increases toward the origin. Redrawn from Tyburczy JA and Roberts JJ (1990) Low frequency electrical response of polycrystalline olivine compacts: Grain boundary transport. *Geophysical Research Letters* 17: 1985–1988.

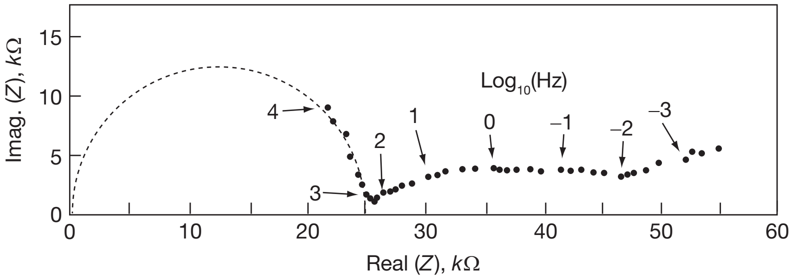

Figure 20 Example of impedance spectroscopy on a sample of San Carlos olivine at 1200 °C and an fO_2 of 10^{-15} Pa. Data are from Tyburczy and Roberts (1990). We have highlighted the highest frequency (10^3–10^4 Hz) mechanism, interpreted as grain-interior conduction, with a 12 kΩ radius arc centered on the real axis. Intermediate frequency (10^{-2} to 10^2 Hz) impedance is associated with grain boundary conduction, and lowest frequency impedance as polarization on the electrode surfaces.

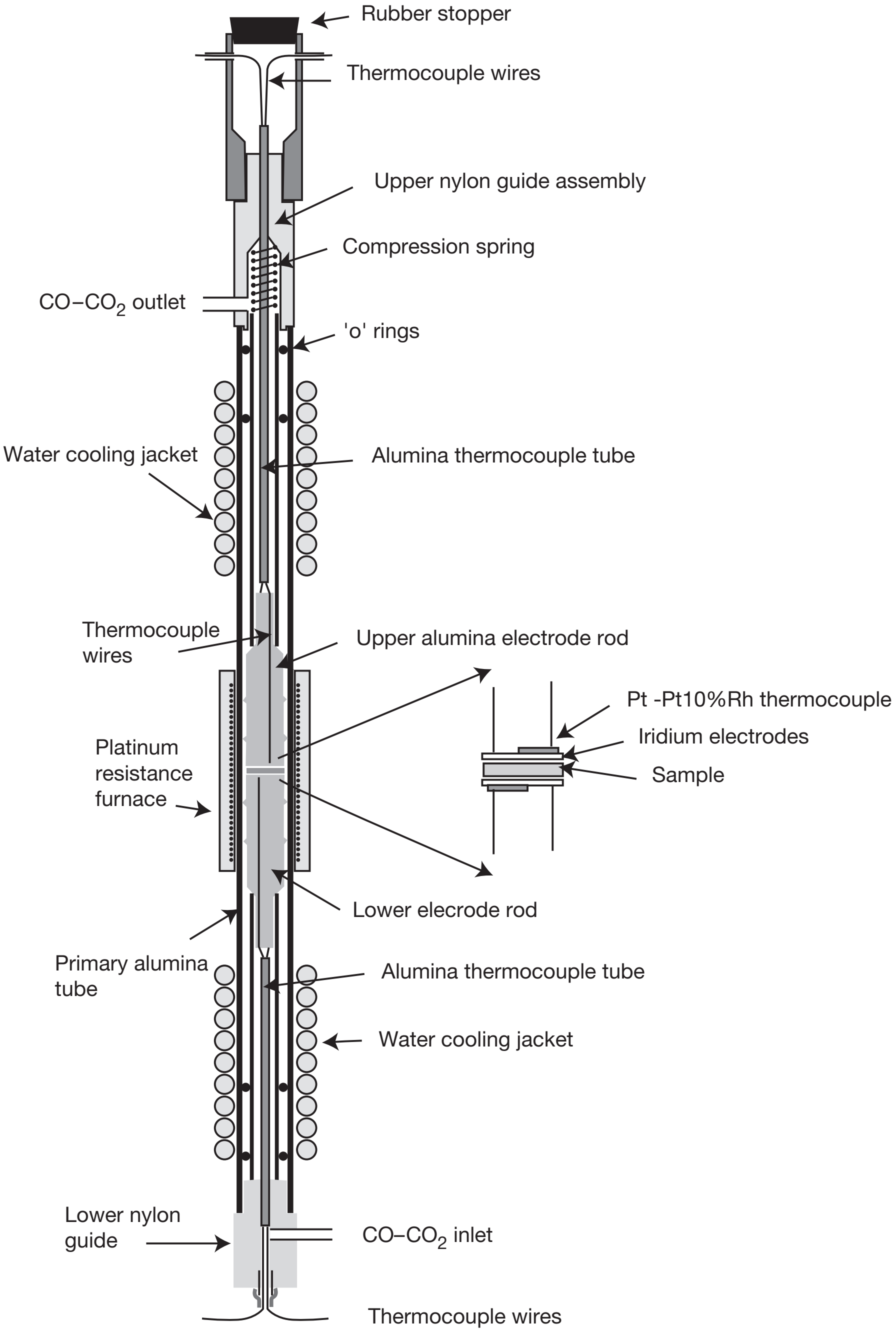

Figure 21 Gas-mixing furnace for making electric conductivity measurements at room pressure and high temperature (after Duba et al., 1990). The mixture of CO and CO_2 is controlled by separate mass flow controllers for each gas. The vertical size is about 60 cm.

designed to control the oxygen activity surrounding the sample and to minimize conduction leakage around the sample. The electrodes in contact with the sample are made of iridium, rather than platinum, to minimize iron loss. The thermocouple leads, which allow the temperature to be measured on both sides of the sample (important for thermopower measurements), also serve as electrode leads for a 2-electrode measurement. For thermopower measurements, the entire assembly can be moved up or down in the furnace/cooling system to create a temperature gradient across the sample.

5.07.4.6 High-Pressure Measurements

The surface pressure gas-mixing furnace is unsurpassed in terms of making measurements under finely controlled fO_2, but if one wishes to examine electric conductivity of lower mantle phases (minerals), these need to be made within a high-pressure apparatus using solid chemical buffers instead of gas mixes.

There are three basic types of high-pressure apparatus. The first is the piston and cylinder apparatus, which is exactly what it says and is suitable only for relatively low pressures, although it does have the advantage that gas mixes could be used to control fO_2. The second is the multianvil cell (Figure 22), which uses a set of carefully shaped steel, tungsten carbide, and/or sintered diamond anvils to turn the force of a 1000+ ton uniaxial press into a triaxial confining pressure of up to several tens of gigapascals (40 GPa is about 1000 km deep). Figure 23 shows a sample capsule used for conductivity measurements of high-pressure olivine phases in a multianvil cell. Finally, the diamond anvil cell allows similar or greater pressures to the multianvil cell with a much smaller experimental setup and the possibility of optical interaction with the specimen. X-ray experiments can be made through the diamond, and lasers used to locally heat the sample (Figure 24).

5.07.4.7 Thermopower Measurements

In a gas-mixing furnace such as shown in Figure 21, the assembly can be moved up or down to produce a temperature gradient across the sample that can then be measured using the two thermocouples. The resulting thermoelectric effect, also known as the Seebeck effect, can be measured as an potential difference between the two electrode wires. The thermopower Q is defined as

$$Q = -\lim_{\Delta T \to 0} \frac{\Delta V}{\Delta T}$$

The mobility of defects is less on the cold side of the sample, and so an excess 'condenses' there. For a charge-carrying defect, this results in an electric field across the sample that can be measured with a suitable high-impedance voltmeter. The sign convention for Q is such that the sign of the thermopower

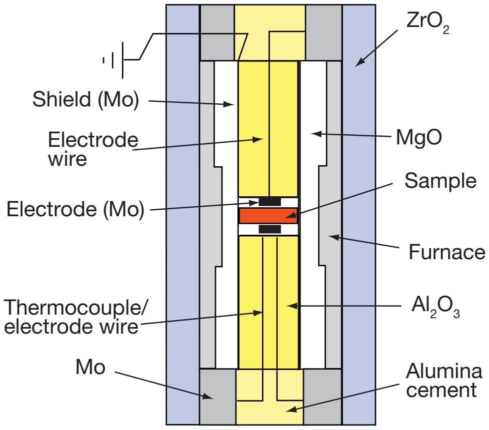

Figure 23 High-pressure conductivity cell for use in a multianvil press. Reproduced from Xu YS, Poe BT, Shankland TJ, and Rubie DC (1998) Electric conductivity of olivine, wadsleyite, and ringwoodite under upper-mantle conditions. *Science* 280: 1415–1418.

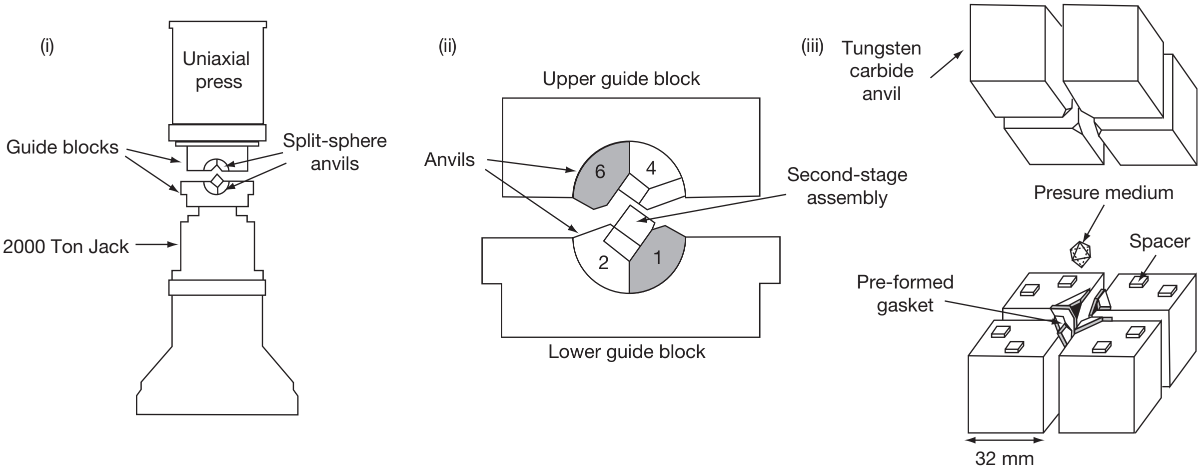

Figure 22 The multianvil cell. From left to right: (i) the uniaxial press and the split-sphere anvils, (ii) close-up of the split-sphere anvils showing the location of the second-stage assembly, and (iii) the second-stage assembly of eight tungsten carbide cubic anvils and an octahedral pressure medium. Reproduced from Libermann RC and Wang Y (1992) Characterization of sample environment in a uniaxial split-sphere apparatus. In: Syono Y and Manghnani MH (eds.) *High Pressure Research: Applications to Earth and Planetary Sciences*, pp. 19–31. Washington, DC: American Geophysical Union.

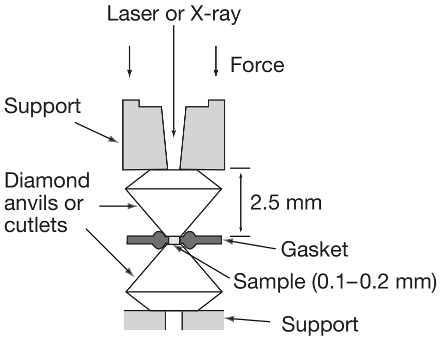

Figure 24 A diamond anvil setup designed to measure precise strains using an optical technique (from Meade and Jeanloz, 1987). The size of the sample area is less than 1 mm in diameter.

agrees with charge-carrying defect. Thermoelectric power is inversely proportional to the concentration of charge carriers and is equivalent to the entropy per charge carrier. Expressions for this are of the form (Tuller and Nowick, 1977)

$$Q = \frac{k}{q}\left[\ln \beta \frac{(1-c)}{c} + \frac{S}{k}\right]$$

Here, c is the fraction of sites that contain a charge carrier, q is the charge of the defect, β is a degeneracy factor (for electrons, β is usually taken to be equal to 2 to account for the two possible spin states), S is the vibrational entropy associated with the ions (usually considered negligible), and k is the Boltzmann constant. Because thermopower is dependent only on concentration, and not on mobility, it provides an important tool for the study of charge transport in minerals.

5.07.4.8 Conductivity of Mantle Minerals

Mantle mineralogy depends to a large extent on the increase in pressure with depth and is inferred from a combination of mantle xenoliths, models of seismic velocity, estimates of bulk chemistry, and high-pressure laboratory studies. Figure 25 shows such a model of mantle mineralogy in pictorial form.

Figure 26 shows laboratory studies of water-free electric conductivity for all the major minerals in the mantle, represented as Arrhenius fits to the original data. Most of these data were collected in a multianvil press, where large (by comparison with diamond anvil cells) samples can be made and solid-state buffers used to control fO_2. Most minerals have activation energies between 0.5 and 2 eV ($1\ \mathrm{eV} = 1.6 \times 10^{-19}\ \mathrm{J\,mol^{-1}}$). It is interesting to note that upper mantle minerals have activation energies of around 1.5 eV, while lower mantle minerals (magnesiowüstite and silicate perovskite) have activation energies of 0.7 eV. Whether there is a reason or not for the high-pressure phases to have lower activation energies, the implication is that the lower mantle will be more uniform in conductivity given similar variations in temperature.

5.07.4.9 Olivine Conductivity

Olivine attracts special attention from the geophysics community because it dominates the mineralogy of the upper mantle, a region that is easiest to study and closest to the crust. Because the next most abundant upper mantle mineral, clinopyroxene, has a conductivity similar to olivine, it is fairly safe to build models of mantle conductivity on studies of olivine.

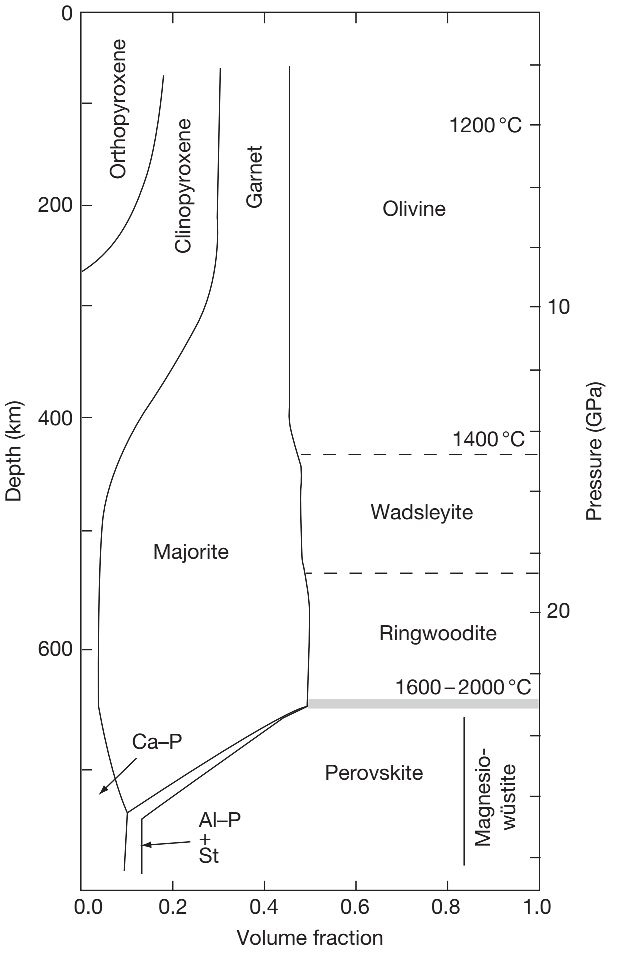

Figure 25 Mantle mineralogy, after Ito and Takahashi (1987). Olivine is the major component of the upper mantle. It is a orthorhombic magnesium iron silicate, $(\mathrm{Mg}_{1-x}\mathrm{Fe}_x)_2\mathrm{SiO}_4$, where x is typically 0.1 in the mantle. Wadsleyite and ringwoodite are high-pressure phases of olivine. Garnets are cubic aluminum silicates of the general composition $\mathrm{X}_3\mathrm{Al}_2\mathrm{Si}_3\mathrm{O}_{12}$, where X can be magnesium (pyrope), divalent iron (almandine), manganese (spessartine), or calcium (grossular) (neglecting garnets where the Al is replaced by other trivalent cations). Majorite is a high-pressure tetragonal phase of $(\mathrm{Mg,Fe})\mathrm{SiO}_3$ garnet. Orthopyroxene is typified by enstatite, $(\mathrm{Mg}_{1-x}\mathrm{Fe}_x)\mathrm{SiO}_3$, a chain silicate of orthorhombic structure. Clinopyroxene is typified by the monoclinic diopside series $\mathrm{Ca(Mg,Fe,Mn)Si}_2\mathrm{O}_6$, another chain silicate. Magnesiowüstite (also called ferropericlase) is magnesium iron oxide $(\mathrm{Mg}_{1-x}\mathrm{Fe}_x)\mathrm{O}$. Stishovite (St) is a high-pressure phase of silica (quartz), or SiO_2. Silicate perovskite is a high-pressure distorted cubic form of magnesium iron silicate, $\mathrm{Mg}_{1-x}\mathrm{Fe}_x\mathrm{SiO}_3$. Ca–P and Al–P are CaO- and $\mathrm{Al}_2\mathrm{O}_3$-rich phases, respectively.

Olivine, an orthorhombic mineral, is mildly anisotropic. Figure 27 shows measurements of olivine anisotropy, made on samples from mantle xenoliths found in San Carlos Apache Indian Reservation, Arizona. The [0 0 1], or c-axis, is the most conductive but still barely more than a factor of 2 greater than the other axes. The [1 0 0] (a) axis is of intermediate conductivity. This is, perhaps, unfortunate, because seismic and

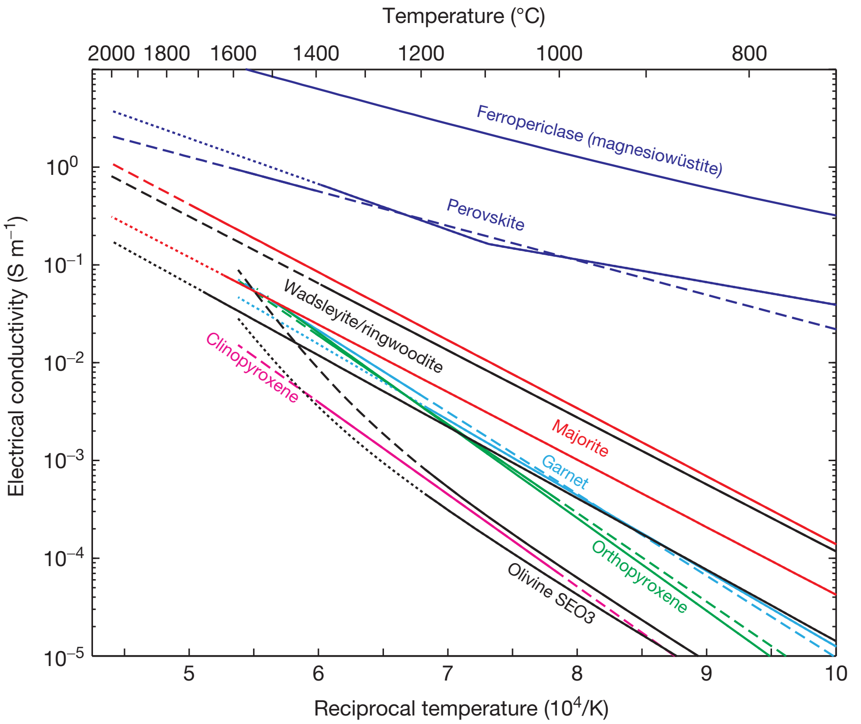

Figure 26 Laboratory studies of conductivity in nominally anhydrous mantle minerals, expressed as Arrhenius model fits to data. Solid lines represent the temperatures over which measurements were made; the broken and dotted lines are extrapolations to higher and lower temperatures. Ferropericlase data (dark blue) are from Dobson and Brodholt (2000). Perovskite results (dark blue) are from Xu et al. (1998, broken line) and Yoshino et al. (2008a, dotted line). Ringwoodite (black) is from Yoshino et al. (2008b, broken line) and wadsleyite (also black) is from Yoshino and Katsura (2012, dotted line). Majorite garnet (red) is from Yoshino et al. (2008c) for a pyrolite composition (dotted line) and mid-ocean ridge basalt composition (broken line). Garnet (light-blue) results are from Xu and Shankland (1999, broken line) and Dai and Karato (2009a, dotted line). Orthopyroxene (green) is from Xu and Shankland (1999, broken line) and Zhang et al. (2012, dotted line). Clinopyroxene (pink) is from Xu and Shankland (1999). Olivine SEO3 is from Constable (2006) for iron–wüstite (black, dotted line) and quartz–fayalite–magnetite (black, broken line) models of mantle oxygen fugacity.

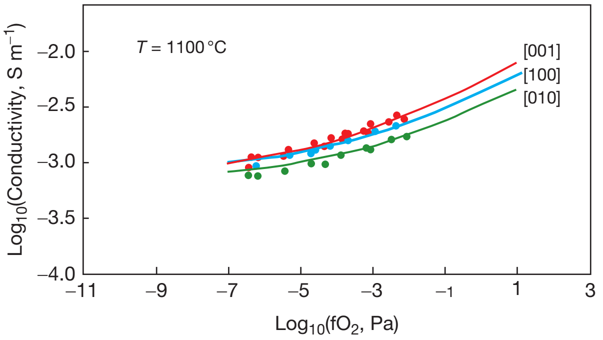

Figure 27 Data (symbols) and model fits (lines) for electric conductivity of San Carlos olivine along the three crystallographic axes as a function of fO_2 at a temperature of 1200 °C (data from Du Frane et al., 2005). Anisotropy is not strong, and the crystal axis most likely to be aligned in the mantle, [1 0 0], is of intermediate conductivity.

deformational models of the upper mantle suggest that this axis will be aligned in the direction of plate motion.

SO2 (Constable et al., 1992) is a quantitative model of olivine conductivity based on a geometric average of high-temperature single-crystal measurements and lower-temperature measurements on polycrystalline olivine rocks (which would melt above 1250 °C, fluxed by the pyroxene content).

The SO2 model is

$$\sigma = 10^{2.40} e^{-1.6\,\text{eV}/kT} + 10^{9.17} e^{-4.25\,\text{eV}/kT}\,\text{S m}^{-1}$$

where the first term corresponds to low-temperature behavior and the second term corresponds to a conduction mechanism that becomes dominant above 1300 °C. SO2 served as a useful benchmark for some time but was often found to underpredict mantle conductivity. A new model, SEO3, was created based on our understanding of the conduction mechanisms in olivine (Constable, 2006). The relationship between the major defect population in olivine and fO_2 is thought to be described by

$$8\text{Fe}_{\text{Mg}}^{\times} + 2\text{O}_2 \rightleftharpoons 2V_{\text{Mg}}'' + V_{\text{Si}}'''' + 4\text{O}_{\text{O}}^{\times} + \text{Fe}_{\text{Mg}}^{\bullet}.$$

Many studies indicate that the dominant charge carriers are $\text{Fe}_{\text{Mg}}^{\bullet}$ and V_{Mg}''. For samples buffered by pyroxene, this model predicts that $[\text{Fe}_{\text{Mg}}^{\bullet}]$ and $[\text{V}_{\text{Mg}}'']$ will each have a dependence on fO_2 of the form

$$\left[\text{Fe}_{\text{Mg}}^{\bullet}\right] = a_{\text{Fe}} f_{\text{O}_2}^{1/6}; \qquad \left[\text{V}_{\text{Mg}}''\right] = a_{\text{Mg}} f_{\text{O}_2}^{1/6}$$

where the preexponential terms a are constant and [] denotes concentration. For mixed conduction, total conductivity is given by

$$\sigma = \sigma_{\mathrm{Fe}} + \sigma_{\mathrm{Mg}}$$
$$= \left[\mathrm{Fe}^{\bullet}_{\mathrm{Mg}}\right]\mu_{\mathrm{Fe}}e + 2\left[\mathrm{V}''_{\mathrm{Mg}}\right]\mu_{\mathrm{Mg}}e$$

where μ are the respective mobilities for the charge carriers and e is the charge on the electron or hole.

Thermopower measurements provide a mechanism of estimating concentration independently of mobility, and Constable and Roberts (1997) created a model of conduction in olivine based on a combined thermopower/conductivity data set. **Figure 28** shows the data set used for this – a dunite from San Quintin in Baja California, Mexico. Natural rocks are useful samples because the crystallographic orientations are usually randomized, and there are enough minor phases to buffer silica. It can be seen that the effect of fO_2 has the same magnitude as a 100 K change in temperature. Iron content also has an effect on polaron conduction, but Fe content in mantle olivines is quite constant at about 10%. This model supports earlier predictions (Schock et al., 1989) that below 1300 °C, small polaron hopping ($\mathrm{Fe}^{\bullet}_{\mathrm{Mg}}$) dominates the conduction mechanism and, above 1300 °C, magnesium vacancies (V''_{Mg}) account for conductivity.

Constable (2006) used the mobilities and concentrations as a function of temperature and fO_2 from the joint conductivity/thermopower model to create a quantitative model of conductivity that is perhaps more reliable at high temperature than SO2 (**Figure 29**), because it is based on the Boltzmann relationships rather than parametric fits to data. Furthermore, it allows explicit designation of the fO_2 conditions; although the quartz–fayalite–magnetite buffer is often used for the upper mantle, it is possible that at depth fO_2 may be lower and close to the iron–wüstite buffer (McCammon, 2005). The effect of pressure is neglected in these models, but Xu et al. (2000) showed that it is small compared with the sample-to-sample variations associated with high-pressure measurements. (In **Figure 29**, the QFM curves are very slightly different than in Constable (2006) because they use the fugacity model of O'Neill (1987) to replace a simpler approximation used in the original paper.)

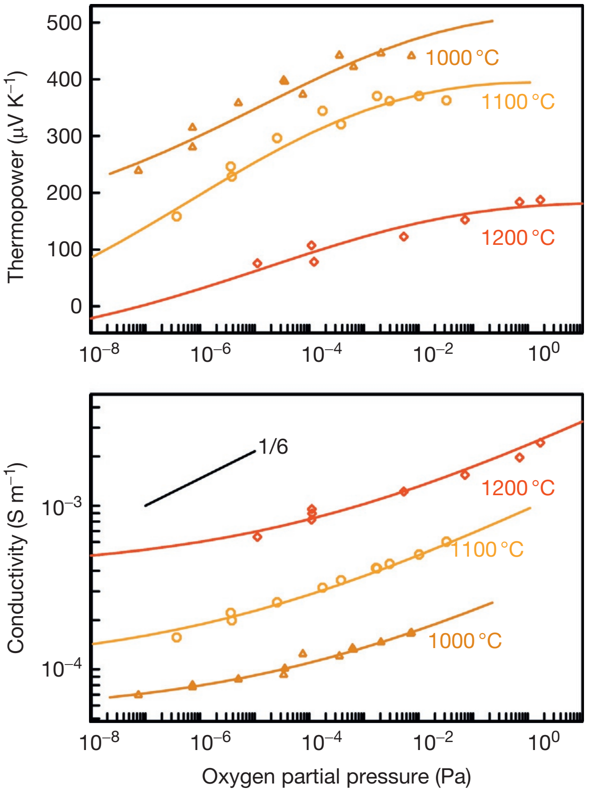

Figure 28 Data (symbols) and model fits (lines) for thermoelectric power and conductivity data for San Quintin dunite, as a function of fO_2 for three temperatures. Reproduced from Constable S and Roberts JJ (1997) Simultaneous modeling of thermopower and electrical conduction in olivine. *Physics and Chemistry of Minerals* 24: 319–325.

5.07.5 Global Conductivity Structure

In this section, we will examine what is known about the electric conductivity of the Earth's interior, from both field measurements and laboratory studies. Field studies include long-period MT soundings using temporary instrument installations, GDS studies using magnetic observatory data, and, most recently, induction studies using magnetic satellite data.

5.07.5.1 The Oceans and Crust

The most significant conductivity feature on the surface of the Earth is the world ocean. Fortunately, the ocean is also the most easy feature to characterize. Global maps of bathymetry are available, and seawater conductivity is well defined as a function of salinity (nearly constant) and temperature. **Figure 30** shows an example of the electric conductivity structure of the upper 1000 m of a site in the Pacific Ocean. The surface water is warm and more than 5 $\mathrm{S\,m^{-1}}$, but both temperature and conductivity drop rapidly below the thermocline, in this case at a depth of about 70 m. By a depth of 1000 m, the conductivity is close to that observed at full ocean depth, and a value of 3.3–3.5 $\mathrm{S\,m^{-1}}$ is usually used to represent ocean conductivity.

The rocks of the oceanic crust are, by and large, also fairly easy to characterize because for the most part, the genesis of oceanic crust is uniform and the metamorphic history fairly simple. Boreholes to a depth of a kilometer or so, along with marine-controlled source EM studies, provide *in situ* measurements of conductivity, which, combined with our knowledge of oceanic geology gleaned from dredging and ophiolite studies, allows us to paint a fairly good picture of electric structure in the oceanic crust (**Figure 31**). Away from ridges, the conductivity is basically a measure of the porosity of the volcanic and igneous rocks that make up the crust. Near ridges conductivity is increased by the presence of magma and hydrothermal fluids in the crust.

In stark contrast, the electric structure of the continental crust (which includes the continental shelves) is very much more complicated, undoubtedly because it is better studied than the oceanic crust, but mostly because the geologic history is much more complicated and the variation in water content (and salinity) is much larger. Data for crustal conductivities on the continents come mainly from broadband and long-period MT soundings, with some data from large-scale controlled-soure

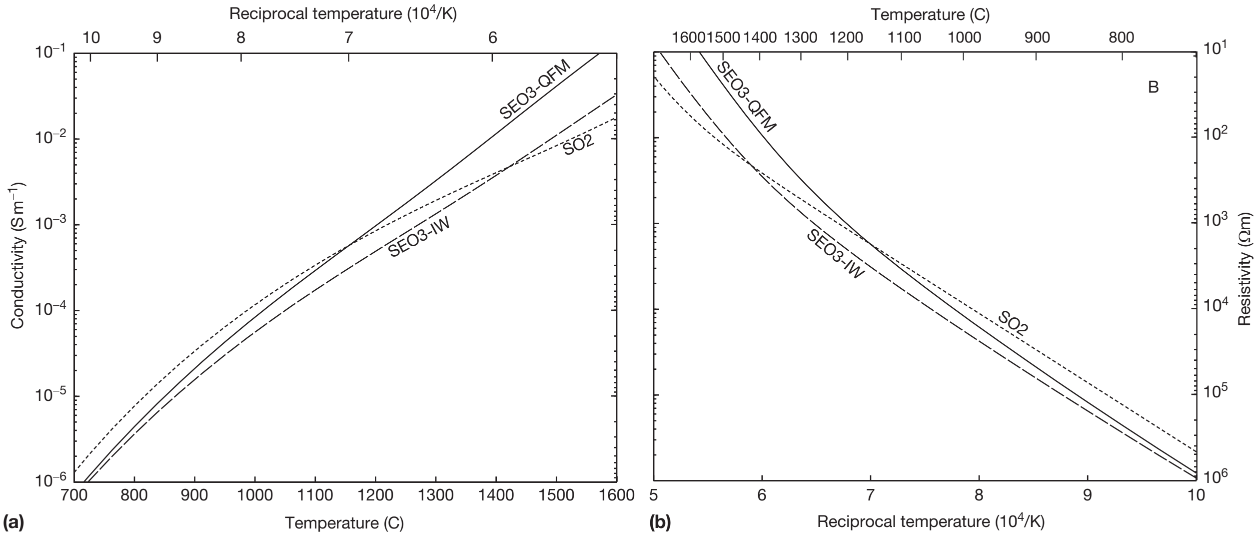

Figure 29 The SEO3 olivine conductivity–temperature model for two different fO_2 conditions, quartz–fayalite–magnetite (SEO3-QFM) and iron–wüstite (SEO3-IW) (Constable 2006). For comparison, the SO2 model of Constable et al. (1992) is also shown. The models are represented in both 1/T space (b) and temperature space (a).

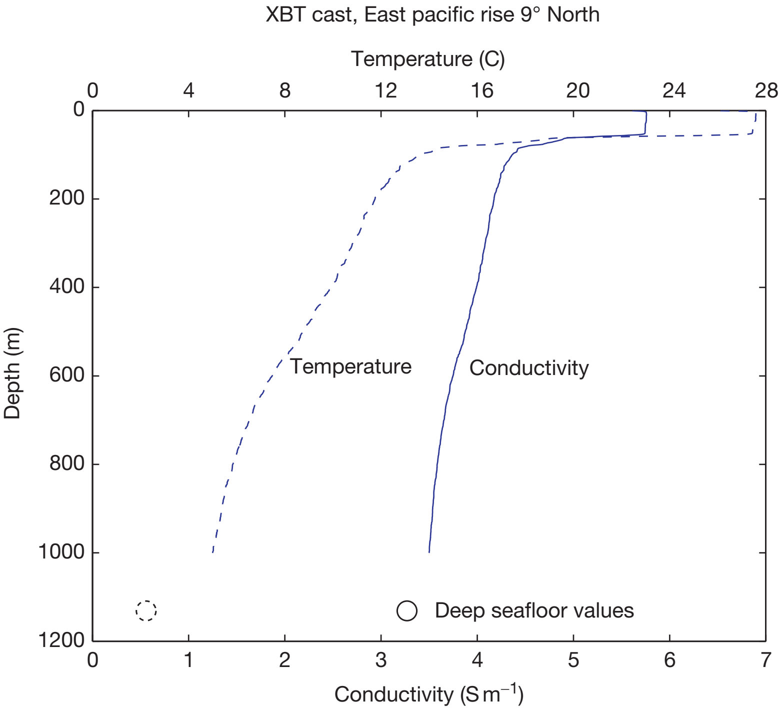

Figure 30 Expendable bathythermograph (XBT) taken in the Pacific Ocean near the East Pacific Rise at 9°N. The temperature profile has been converted to electric conductivity. The 'o' symbols show the values near the seafloor in the deeper ocean (4000–5000 m).

electromagnetic (CSEM) and resistivity studies. However, neglecting important details and ignoring unusually conductive, volumetrically small, and often economically significant minerals, we can make some gross generalizations:

- Continental shields: 10^3–10^6 Ωm
- Continental sediments: 10–100 Ωm
- Marine sediments: 1–100 Ωm.

Everett et al. (2003) formalized this approach to generate a global crustal conductance map, using the global sediment thickness map of resolution of 1° × 1° compiled by Laske and Masters (1997). This map contains sediments discretized in up to three layers: a surface layer up to 2 km thick, an underlying layer up to 5 km thick, and, where necessary, a third layer to make up total sediment thickness, which often exceeds 10 km. The sediment map was augmented by a 1° × 1° topographic/

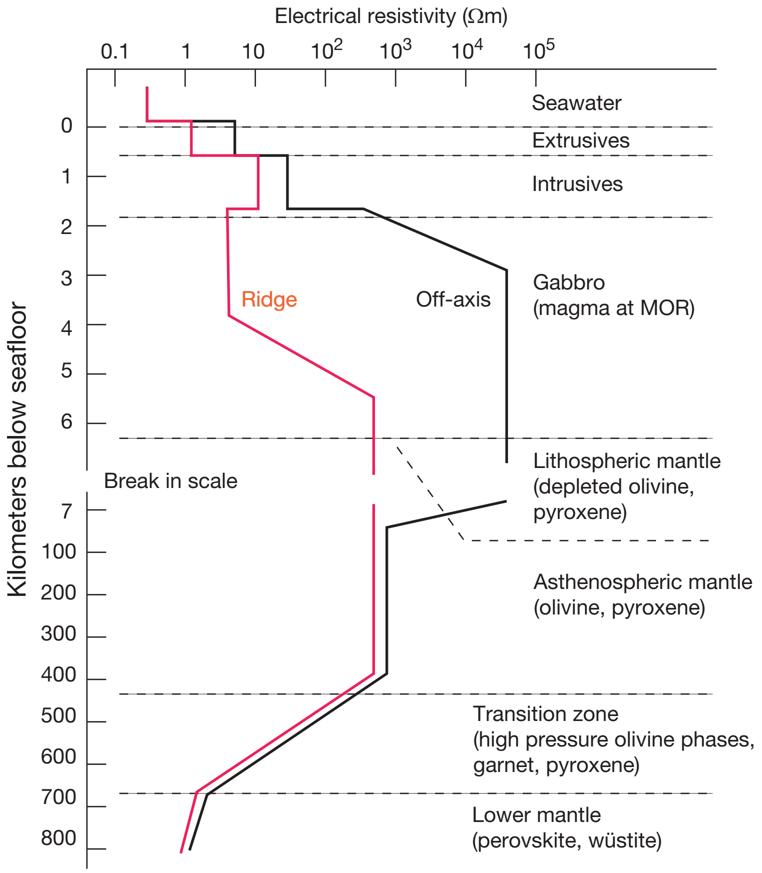

Figure 31 Electric conductivity structure of the oceanic crust and mantle, based on marine CSEM to depths of about 50 km and marine MT below that.

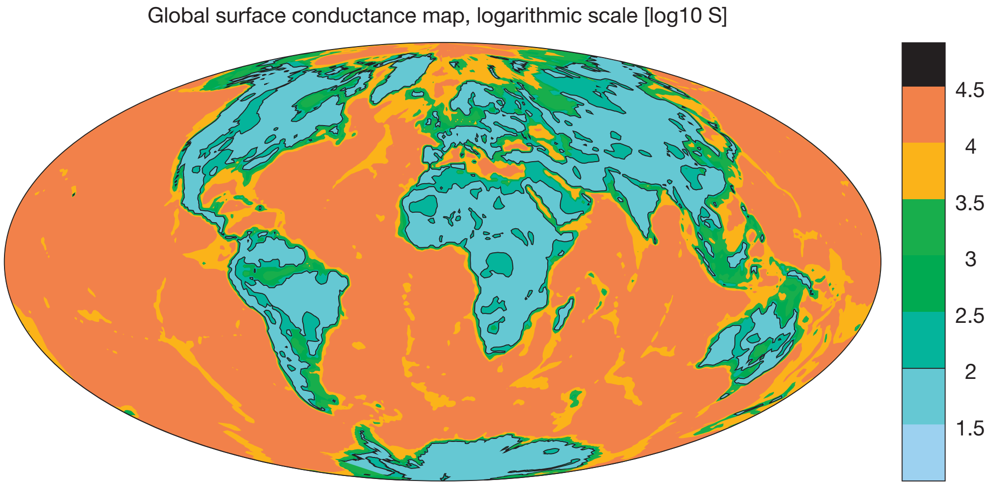

Figure 32 Global electric conductance generated by the crustal algorithm of Everett et al. (2003).

bathymetric map. Continental and oceanic sediments were mapped heuristically to conductivity and summed over depth to create a surface conductance map (Figure 32). The previously mentioned algorithm is undoubtedly arbitrary and could be improved upon but improves on simple ocean depth as a proxy for conductance. Overall, the sedimentary sections defined in this way contribute only 10% to the total surface conductance, but in areas such as the Gulf of Mexico, Arctic Ocean, and Mediterranean/Caspian/Black Sea, accumulated sediment has a conductance comparable to the oceans and sediments drastically alter the shape of the continent/ocean function.

For frequencies where the skin depth is large compared with the thickness of a layer, a surface layer can be characterized by its conductance only, because its thickness cannot be resolved and attenuation of EM energy is determined entirely by the conductivity–thickness product, or conductance. Computations in three dimensions often exploit this phenomenon using a thin-sheet algorithm (e.g., Kuvshinov et al., 1999).

5.07.5.2 The Mantle

As can be seen from **Figure 11**, global response functions from satellite and observatory measurements are in broad general agreement. This is further illustrated in **Figure 33**, which shows the data set used in an inversion study by Medin et al. (2006). These data consist of a combination of stacked global observatory GDS responses (Constable, 1993a), which relied on assumptions of P_1^0 geometry, and European observatory responses of Olsen (1999), which allowed more complicated source-field geometry and thus a broader bandwidth. Medin et al. excluded four admittances that failed to satisfy the assumption of one dimensionality, three of which they had reason to believe did not meet the source-field requirements.

Figure 34 shows various inversions of this data set. The green lines represent the D^+ model of Parker and Whaler (1981), scaled by 10^5 and fitting the data to RMS 1.044. The red line is a smooth, first-derivative regularized inversion fitting the data to RMS 1.2, and the blue line is a similar inversion but allowing unpenalized jumps at the 440 and 670 km seismic discontinuities. Finally, the yellow boxes are bounds on average conductivity at the 90% confidence level over the depth intervals 0–418, 418–672, and 672–1666 km, derived by Medin et al. (2006). The broader bounds put no restrictions on the models, and the tighter bounds shown in the darker color restrict the models to be monotonically increasing in conductivity with depth.

These models are representative of the many mantle conductivity profiles published in the literature and are in good agreement with the anhydrous mineral conductivities shown in **Figure 26**. One of the most well-resolved features is the jump in conductivity to 2–3 S m^{-1} in the lower mantle, entirely consistent with the laboratory measurements on silicate perovskite. The order of magnitude increase in conductivity in the lowermost mantle is just within the range of thermally activated conduction in perovskite or could be the influence of other mineral phases. However, this increase in model conductivity is poorly constrained, relying on the longest-period measurements having largest uncertainty, and probably represents a lower bound on conductivity because the smoothness penalty minimizes slope. The order of magnitude increase of conductivity in the transition zone is in general agreement with the more recent water-free laboratory measurements on the high-pressure phases wadsleyite and ringwoodite.

The uppermost mantle above the transition zone is likely to be quite heterogeneous and dependent on local tectonic setting, and although Medin et al.'s data are all derived from land observatories and thus avoid the oceans, the continental crust can be locally quite conductive. This part of the model is the least likely to have a monotonically increasing conductivity, especially if fO_2 decreases with depth, but the bounds on average conductivity span the range for dry olivine conductivity. While one-dimensional global response functions are in general agreement with each other and with laboratory studies, individual response functions vary considerably (e.g., Egbert and Booker, 1992; Lizarralde et al., 1995; Schultz et al., 1993; Tarits et al., 2004), with nearly two orders of magnitude

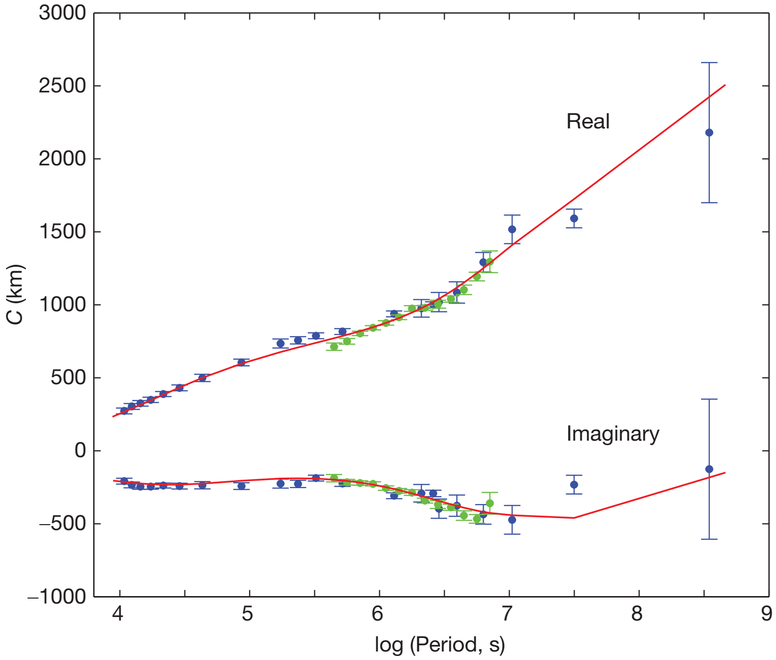

Figure 33 Response function used by Medin et al. (2006), consisting of the slightly edited data sets from Olsen (1999, blue symbols) and Constable (1993a, green symbols). The error bars are as reported by the authors. The red line is the response of the smooth model shown in **Figure 34**, fitting the data to a conservative RMS 1.2.

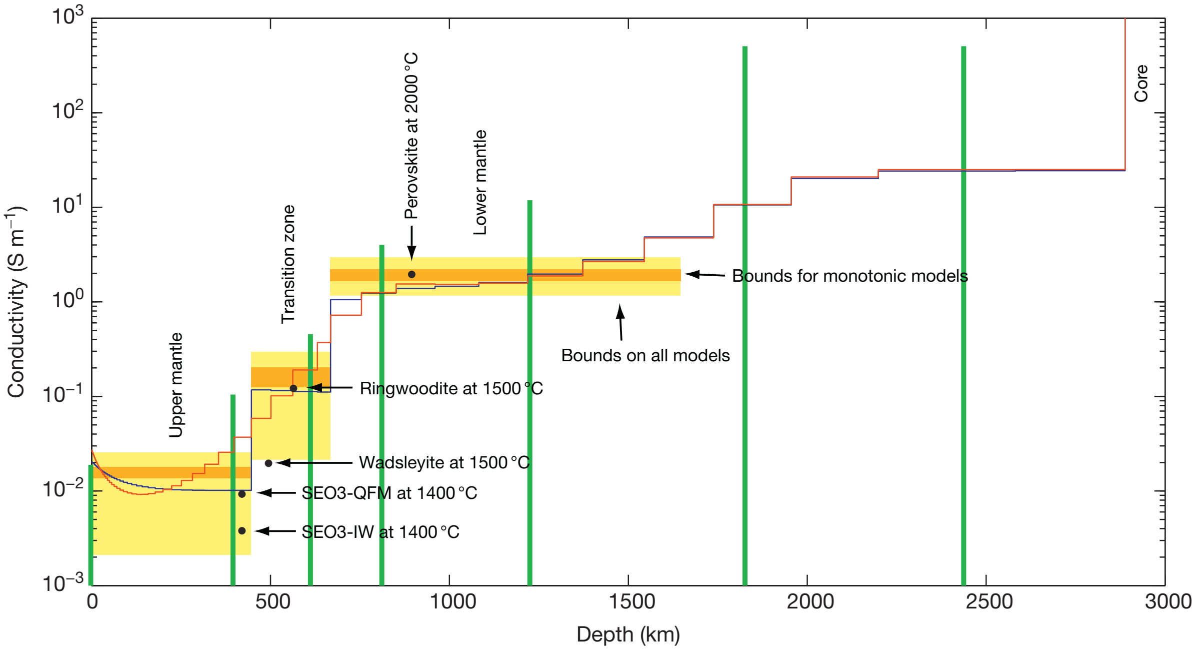

Figure 34 Models fitting the data set shown in **Figure 33**. Green lines are the D^+ model divided by 10^5, red line is a first-derivative maximally smooth model, and the blue line is a smooth model that is allowed to jump at 440 and 670 km. The yellow boxes represent bounds on average conductivity from Medin et al. (2006). Values of selected mineral conductivities from **Figure 26** are also shown.

variation in conductivity inferred for the upper mantle. This, of course, begs the question of the reliability of the response functions, particularly for single-site MT soundings where galvanic distortions of the electric field and effects of 2D and 3D structure are not all that unusual. Certainly, early single-site MT measurements carried out in the deep ocean basins were distorted by the effect of coastlines (Heinson and Constable, 1992). However, there are several factors that could modify the conductivity of the upper mantle from the averages presented earlier in the text and that may become the dominant conduction mechanism locally.

5.07.5.2.1 Melt

Since magma is very much more conductive than subsolidus olivine, one mechanism for increasing conductivity is to invoke a mantle permeated by partial melt. Tholeiitic melt conductivity is more than 1 S m^{-1}. For small melt fractions to be an effective mechanism for increased conduction, the melt must be well connected. However, well-connected melt is gravitationally unstable and will migrate upward, and so while partial melt is clearly an important mechanism in volcanic systems and mid-ocean ridges, it must be replenished on a timescale comparable to the residency time in the mantle for it to contribute to permanent enhancement of conductivity or be trapped by a freezing horizon. Naif et al. (2013) inferred just such trapping of a few percent melt at the lithosphere–asthenosphere boundary in the 23 Myr old Cocos plate offshore Nicaragua, based on an interpretation of marine MT data. It is unlikely that melt will persist in much older oceanic mantle, but this result suggests that it may be common under young oceanic lithosphere.

It has been recently shown that carbonate melts in peridotite are more than an order of magnitude more conductive than silicate melts (Gaillard et al., 2008; Yoshino et al., 2012). Furthermore, carbonate melts have low dihedral angles, which results in high wetting of grain surfaces and high interconnection, and the presence of CO_2 decreases the melting point of peridotite, allowing melting to occur at greater depths in the mantle upwelling beneath mid-ocean ridges. This all means that significant increases in deep mantle conductivity are possible from small fractions of carbonate melting in peridotite. Key et al. (2013) claimed to have observed such an increase at a depth of 140 km beneath the mid-ocean ridge that separates the Pacific and Cocos plates.

5.07.5.2.2 Carbon

Graphite is extremely conductive (10^4–10^6 S m^{-1}), and so it would take only a small amount to increase mantle conductivity over that of dry olivine, as long as it is well connected. The idea that carbon might contribute to mantle conductivity was first put forward by Duba and Shankland (1982). There is a significant amount of carbon in the mantle (several hundred parts per million) that can exist as CO_2 fluids or graphite. Movement between the two phases depends on fO_2, and so it is conceivable that CO_2 fluids permeating grain boundaries could be reduced to form a connected network of graphite. However, recent results of Watson et al. (2010) for 0.1 wt.% carbon in polycrystalline olivine suggest that at these concentrations, carbon does not form a connected network or film and, indeed, slightly increases resistivity by acting in series with olivine conduction. Another limitation on carbon as a conduction mechanism for mantle rocks is that below about 160 km, graphite turns into diamond, which is a nonconductor. Note also that carbon has a low thermal activation energy, so we would not expect to see an increase in conductivity with temperature and depth for carbon-enhanced conductivity.

5.07.5.2.3 Strain-induced defects

Since the early marine MT studies inferred a zone of increased conductivity at the depth of the asthenosphere, one possibility that was considered was that straining generated defects that contribute to conduction. This idea was dispelled by careful measurements by Hirsch and Wang (1986), and now, it is clear that marine MT measurements may be interpreted in terms of lower conductivities by taking into consideration the effect of the coastlines (Heinson and Constable, 1992; Key and Constable, 2011).

5.07.5.2.4 Water

Like carbon, water is known to exist in the mantle – estimates are that several Earth oceans are still resident somewhere in the deep Earth. Where, and in what state, is less well understood.

There are three ways to store water in the mantle: free water, hydrous minerals, and as defects in nominally anhydrous minerals. Free water could exist for a period of time in the coolest parts of the mantle but, at even modest temperatures, will eventually react with olivine to create serpentine minerals. This mechanism is interesting in that magnetite is excluded during the reaction, potentially creating halos around relic olivine grains of fine magnetite that potentially can be electrically connected to lower the resistivity of the rock considerably (Stesky and Brace, 1973). However, hydrous minerals are not otherwise conductive (consider mica). At some temperature/pressure, depending on the mineral but generally at depths shallower than 125 km, hydrous minerals will decompose to produce free water, which will usually lower the melting point sufficiently to generate a partial melt into which water dissolves, and the melt in turn will be gravitationally unstable and migrate upward. This mechanism is largely responsible for volcanism at subduction zones.

The idea that water dissolved as point defects in olivine could enhance electric conductivity was originally proposed by Karato (1990), based on observations that chemical diffusion of hydrogen in olivine was very high, particularly along the a-axis. The activation energy of diffusion is 1.3 eV, similar to other upper mantle conduction mechanisms. Although initially put forward as an explanation for early marine MT measurements, the idea found a broad and enthusiastic following in the EM community. Since the olivine a-axis is considered to be aligned with mantle flow, conduction by hydrogen as proposed by Karato would create significant anisotropy (only about 100 ppm hydrogen is required to increase a-axis conductivity by an order of magnitude if Karato's diffusion model was correct), and evidence of electric anisotropy in the mantle was often interpreted as support for the hydrogen conduction hypothesis (e.g., Simpson and Tommasi, 2005).

However, the effect of hydrogen on upper mantle conductivity rapidly became a matter for debate. Karato (1990) only considered fast diffusion along the a-axis, but the effect is not as dramatic when the other two axes are taken into account; adding about 1000 ppm hydrogen per silicon atom predicts a conductivity based on diffusivity only slightly above that of dry olivine (Constable, 1993b). While observation of anisotropy in MT data has quickly led to support for the idea of hydrogen conduction, many things can result in anisotropic MT responses; for example, structural anisotropy outside the study area could be difficult to identify without adequate data (e.g., Heinson and White, 2005).

Direct laboratory evidence for enhanced conduction by hydrogen was slow to appear and initial reports were in poor agreement with each other and with the diffusion data (e.g., Poe et al., 2005; Shankland and Duba, 1997; Wang et al., 2006; Yoshino et al., 2006), suggesting that hydrogen does not behave as a simple charged defect in olivine. More recent results have not completely resolved this issue, and there is an order of magnitude or more discrepancy between various studies (**Figure 35(a)**). Yoshino et al. (2009) argued that the higher temperatures used by Wang et al. resulted in dehydration and increased conductivity from water on grain boundaries or the sample cell. Poe et al. (2010) also cited differences in the way water content is estimated and the type of calibration used for this, arguing that a factor of 4 difference with Yoshino et al.'s result could be explained in this way. However, Wang et al. (2006) used the same analytic method as Yoshino et al. (2006, 2009) and still obtained differing results. Poe et al. also noted other differences in sample type and pressure. Because the activation energy for the hydrated samples is lower than for dry olivine, the influence of water will decrease with temperature (and depth). The few results on other hydrated upper mantle minerals, garnet and pyroxene (**Figure 35(b)**), show a similar pattern.

High-pressure measurements on the transition zone minerals ringwoodite and wadsleyite suggest that water solubility in these minerals is very much higher than in upper or lower mantle minerals, leading Bercovici and Karato (2003) to suggest a water-saturated transition zone (410–670 km deep) and pooling of water and melt at the 410 km discontinuity. Furthermore, Huang et al. (2005) showed that conductivity is enhanced by the addition of water in these minerals. This presents the exciting possibility that electromagnetic methods can provide important constraints on deep Earth processes. Based on conductivity bounds obtained from a rigorous analysis of global response function data, Medin et al. (2006) estimated that the global average water content in the transition zone is $<0.27\%$, less than the 0.4% required for pooling at the 410 km discontinuity. However, there remains the possibility that the effect of water is heterogeneous and more significant locally (e.g., Toffelmier and Tyburczy, 2007), and Medin et al.'s inferences depend critically on the early laboratory data. More recent laboratory work (**Figure 35(c)** and **35(d)**), however, echoes the olivine story; different groups and laboratories produce results that differ by up to an order of magnitude. Again, Yoshino et al. produced lower conductivity results and caution against making measurements at high temperatures where water is more labile.

5.07.5.2.5 Oxides and sulfides

Mantle rocks typically contain about one percent oxides of iron, chromium, and titanium, but as discrete crystals, these do not contribute to bulk conductivity in spite of their high mineral conductivities. It is possible to increase the magnetite content of mantle rocks by hydration, as discussed in the preceding text, but there is no field evidence of increased mantle conductivity as a result of this alteration.

Ducea and Park (2000) interpreted high mantle conductivities under western North America as connected sulfide melts

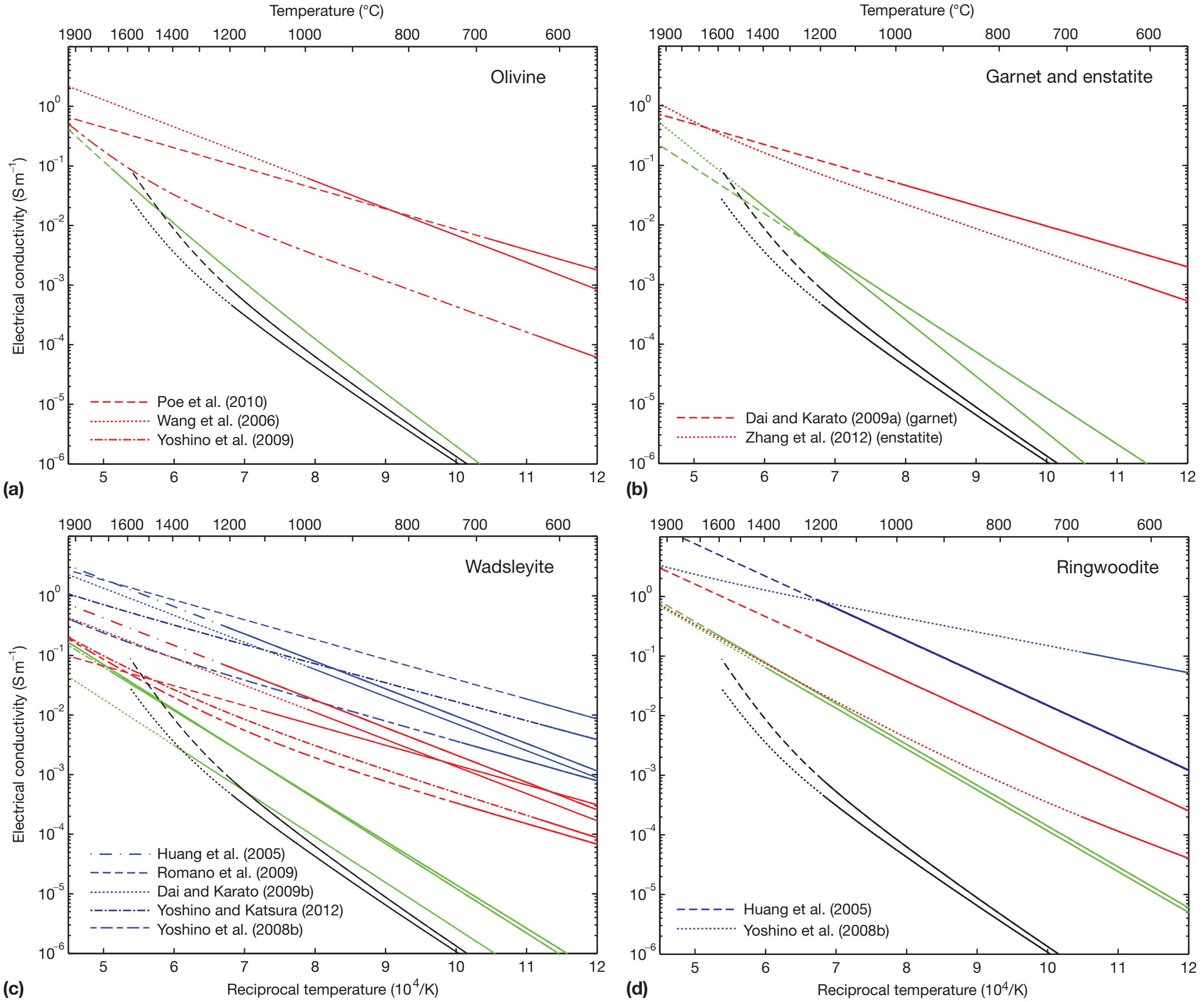

Figure 35 Laboratory studies of conductivity of mantle minerals under pressure, containing 0.1 wt.% water (red) or 1 wt.% water (blue) as point defects, and shown as Arrhenius model fits to data. Green curves are for anhydrous models. Solid lines represent the temperatures over which measurements were made; other lines are extrapolations to higher and lower temperatures. In all plots, the black lines are the SEO3 models shown in **Figure 26**, shown to provide a common reference. (a) Olivine models are from Wang et al. (2006), Poe et al. (2010), and Yoshino et al. (2009). Anhydrous data are from Yoshino et al. (2009). (b) Other upper mantle minerals are from Dai and Karato (2009a) and Zhang et al. (2012). (c) Wadsleyite is from Huang et al. (2005), Romano et al. (2009), Dai and Karato (2009b), Yoshino et al. (2012), and Yoshino et al. (2008b). Dry models are from Romano et al. (2009), Yoshino et al. (2008b), and Yoshino et al. (2012). (d) Ringwoodite is from Huang et al. (2005) and Yoshino et al. (2008b).

at concentrations of less than 0.4 vol.%. Watson et al. (2010) showed that even at 1 vol.%, iron sulfide in polycrystalline olivine was largely unconnected, consistent with estimated percolation threshold of 4–6 vol.%. However, they did observe an increase in conductivity to about $0.1\ \text{S m}^{-1}$ at 900 °C, inferred to be the result of a very small amount of interconnection or an increase in the surface conduction of olivine grains. This is sufficient to explain many observations of increased mantle conductivity that have traditionally been interpreted as melt or the effect of water.

5.07.5.3 The Core

The state of the art with regard to conductivity of the core is nicely summarized in a paper by Stacey and Anderson (2001). Their estimates are $2.1\times10^{-6}\,\Omega\,\text{m}$ in the outer core and $1.6\times10^{-6}\,\Omega\,\text{m}$ in the inner core. Although this refinement on the previously accepted values ($1\text{–}3\times10^{-6}\,\Omega\,\text{m}$) is not terribly significant in terms of geoelectromagnetism, it is important with respect to thermal conductivity, which is linearly related to electric conductivity.

The resistivity of metals increases with temperature because lattice vibrations (phonons) can be considered to scatter electrons. Similarly, adding impurity atoms also increases scattering and resistivity. This is important because we know the outer core is alloyed with 10–25% light elements for the alloyed iron to match density estimates. Stacey and Anderson argued that the effects of impurities are independent of temperature and indeed somewhat independent of the actual impurity chemistry; the effects of Si and Ni (both probably present in the core) are considered similar when measured in weight percent.

Iron behaves as an ideal metal in that the effect of pressure acts to decrease lattice vibrations in a way that affects melting point and resistivity similarly, and so iron at the melting point T_M is expected to have the same resistivity ($1.35\times10^{-6}\,\Omega$ m) whether at zero pressure or at core pressure. At other temperatures T, for a given pressure, resistivity is assumed to be proportional to T/T_M. Thus, at the core–mantle–boundary (CMB), temperature is estimated to be 3750 K and iron solidus as 4147 K, so the component of pure iron resistivity is $\rho=3750/4147\times1.35\times10^{-6}\,\Omega$ m or $1.22\times10^{-6}\,\Omega$ m.

At the inner core boundary, temperature is estimated to be 4971 K and iron solidus as 6000 K, so the component of pure iron resistivity is $1.12\times10^{-6}\,\Omega$ m.

Because iron converts from body-centered cubic (bcc) to hexagonal close-packed (hcp) under pressure, the measurements of iron with impurities have been carried out using shock-wave experiments, in which a gas/explosive gun or laser is fired at a sample. The shock front, moving at velocity u_s, separates material at the starting density, pressure, and temperature (ρ_o, P_o, T_o) with material at the shocked conditions (ρ, P, T). The shock front is supersonic and so moves faster than the actual material, or sound, speed u_p. Conservation of mass across the shock front gives

$$u_s\rho_o=\rho(u_s-u_p)$$

so the density increase produced by the shock is

$$\frac{\rho}{\rho_o}=\left(1-\frac{u_p}{u_s}\right)^{-1}$$

and the pressure is given by the rate of change of momentum per unit area of shock front, which for material starting at rest and room pressure is

$$P=\rho_o u_s\times u_p$$

Hence, knowing the ratio and product of the two velocities for various-sized shocks gives density as a function of pressure for the material. The shock compression is not adiabatic because the material gains kinetic energy. The temperature curve that the material follows during shocking is called a Hugoniot.

Stacey and Anderson (2001) fitted linear models to shock-wave data to conclude that a silicon impurity of volume fraction X would contribute $3.0X\times10^{-6}\,\Omega$ m to resistivity. They expected the silicon to exsolve in a similar way to nickel and so took averages of the two components to finally come up with an impurity contribution of $0.9\times10^{-6}\,\Omega$ m for a total resistivity of $2.1\times10^{-6}\,\Omega$ m. They estimated a lower impurity content for the inner core to derive a total resistivity of $1.6\times10^{-6}\,\Omega$ m.

5.07.6 Conclusions

General agreement between various globally averaged response functions estimated from both satellite and observatory data (**Figures 11** and **33**) has produced a convergence in our understanding of radial electric conductivity structure, represented to a large extent by **Figure 34**. The challenges for the future lie in extending this work to higher dimensions and bounding the amount of water that resides in the upper mantle and transition zone.

5.07.6.1 3D Conductivity from Satellite Data

While there has been a convergence of globally averaged response functions, the ultimate goal of using satellite data is to obtain information about 3D structure in the mantle. This presents challenges both for response function estimation and inversion of data. The induction signal in satellite data is buried deeply in signals from the main field, lithosphere, etc., and the data themselves are not always nicely behaved, having significant gaps and sometimes not having the best control on sensor orientation. One can average through these problems when assumptions of P_1^0 geometry are made and a global 1D response is sought, but the generation of 3D response functions will require a finer control over data quality and response function estimation and dealing with significant complications of source-field morphology, such as the effect of the ionosphere and non-P_1^0 behavior of the magnetosphere. The multi-satellite SWARM experiment should assist greatly in this regard. Also, one needs inversion schemes that are not only fully 3D, but can handle the surface conductivity structure accurately. The problem is that the average conductance of the upper mantle ($0.01\ \mathrm{S\ m^{-1}}\times400\ \mathrm{km}=4000\ \mathrm{S}$) is less than that of the average ocean ($3\ \mathrm{S\ m^{-1}}\times4\ \mathrm{km}=12\,000\ \mathrm{S}$). The more resistive continents provide windows into the mantle, and regions such as mid-ocean ridges, subduction zones, and plumes are likely to be more conductive than the average, but the existence of a surface conductance that varies by nearly four orders of magnitude puts a great demand on the combination of response function estimation and modeling that is needed before 3D mantle structure can be determined.

5.07.6.2 Water in the Mantle

As can be seen from **Figure 34**, while bounds on average mantle conductivity encompass the measured conductivity of anhydrous minerals, an increase in the conductivity of the upper mantle and transition zone (perhaps a factor of 2 or 3) is compatible with the data, if not required by them. Water is commonly invoked to account for this, but since the laboratory experiments on hydrous minerals differ by up to an order of magnitude (**Figure 35**), it is difficult to make a quantitative interpretation of the observations. There have also been recent papers suggesting that carbonate melts or sulfide minerals might easily be responsible for increased conductivity in the upper mantle, obviating the need to invoke conduction by hydrogen. It is important to note that one cannot invoke water concentrations of more than a few hundred parts per million to explain mantle conductivity without then considering the likelihood and effect of consequent melting (e.g., Ardia et al., 2012).

The current proposals for water pooling in the transition zone provide a great opportunity for geomagnetic induction methods to make fundamental contributions to our understanding of the mantle. Although, based on average conductivity, a case can be made that water pooling does not occur, there is every reason to believe that the distribution of water is not homogeneous and that locally water may reach the critical threshold. Long-period MT soundings, if they can be made free of distortions due to large-scale crustal structures, could provide important constraints on this hypothesis. Satellite and observatory response functions, if generated in a way that does not reject 3D structure, could also be brought to bear on this problem.

5.07.6.3 Anisotropy Measurements

A measurement of bulk conductivity tells us only a small amount about the interior of the Earth; the trade-offs between composition and temperature are large and often poorly constrained. A measurement of electric anisotropy, however, unfolds another dimension in our understanding. For example, strain induced by plate motion could generate anisotropy associated either with mineral texture and fabric or by aligning crystallographic axes. Some conduction mechanisms, such as the diffusion of hydrogen in olivine, predict significant anisotropies in the upper mantle. Combining the interpretation of electric measurements with other geophysical data, such as seismic velocity, has always been a good idea, and the combination of electric and seismic anisotropy could prove to be a powerful tool for understanding Earth processes. The reader is referred to a review by Eaton and Jones (2006) and the papers in that volume. However, the challenge here is to make a meaningful measurement of mineralogical or fabric anisotropy and not become confused with anisotropy associated with larger-scale structures.

Acknowledgment

This contribution was supported in part by funding from NASA grant NAG5-13747 and NSF grant EAR-1112861.

References

Alexandrescu MM, Gibert D, Le Mouel JL, Hulot G, and Saracco G (1999) An estimate of average lower mantle conductivity by wavelet analysis of geomagnetic jerks. *Journal of Geophysical Research* 104: 17735–17745.

Ardia P, Hirschmann MM, Withers AC, and Tenner TJ (2012) H_2O storage capacity of olivine at 5–8 GPa and consequences for dehydration partial melting of the upper mantle. *Earth and Planetary Science Letters* 345–348: 104–116.

Avdeev DB (2005) Three-dimensional electromagnetic modelling and inversion from theory to application. *Surveys in Geophysics* 26: 767–799.

Backus GE (1983) Application of mantle filter theory to the magnetic jerk of 1969. *Geophysical Journal of the Royal Astronomical Society* 74: 713–746.

Backus GE and Gilbert JF (1967) Numerical applications of a formalism. *Geophysical Journal of the Royal Astronomical Society* 13: 247–276.

Backus GE and Gilbert JF (1968) The resolving power of gross Earth data. *Geophysical Journal of the Royal Astronomical Society* 16: 169–205.

Backus G, Parker R, and Constable C (1996) *Foundations of Geomagnetism*. Cambridge: Cambridge University Press.

Bahr K, Olsen N, and Shankland TJ (1993) On the combination of the magnetotelluric and the geomagnetic depthsounding method for resolving an electrical conductivity increase at 400 km depth. *Geophysical Research Letters* 20: 2937–2940.

Balasis G and Egbert GD (2006) Empirical orthogonal function analysis of magnetic observatory data: Further evidence for non-axisymmetric magnetospheric sources for satellite induction studies. *Geophysical Research Letters* 33: L11311.

Banks RJ (1969) Geomagnetic variations and the electrical conductivity of the upper mantle. *Geophysical Journal of the Royal Astronomical Society* 17: 457–487.

Barlow WH (1849) On the spontaneous electrical currents observed in wires of the electric telegraph. *Philosophical Transactions of the Royal Society of London* 139: 61–72.

Bercovici D and Karato SI (2003) Whole-mantle convection and the transition-zone water filter. *Nature* 425: 39–44.

Cagniard L (1953) Basic theory of the magneto-telluric method of geophysical prospecting. *Geophysics* 18: 605–635.

Chapman S (1919) The solar and lunar diurnal variations of terrestrial magnetism. *Philosophical Transactions of the Royal Society of London (A)* 218: 1–118.

Chapman S and Bartels J (1940) *Geomagnetism*. Oxford University Press.

Chave AD, Thomson DJ, and Ander ME (1987) On the robust estimation of power spectra, coherences, and transfer-functions. *Journal of Geophysical Research* 92: 633–648.

Clement KT (1860) Das grosse Nordlicht in der Nacht zum 29. Aug. 1859 und die Telegraphenverwirrug in Nord-Amerika und Europa, p. 121. Hamburg.

Constable SC (1993a) Constraints on mantle electrical conductivity from field and laboratory measurements. *Journal of Geomagnetism and Geoelectricity* 45: 707–728.

Constable SC (1993b) Conduction by mantle hydrogen. *Nature* 362: 704.

Constable S (2006) SEO3: A new model of olivine electrical conductivity. *Geophysical Journal International* 166: 435–437.

Constable S (2013) Review paper: Instrumentation for marine magnetotelluric and controlled source electromagnetic sounding. *Geophysical Prospecting* 61: 505–532.

Constable CG and Constable SC (2004a) Satellite magnetic field measurements: Applications in studying the deep Earth. In: Sparks RSJ and Hawkesworth CT (eds.) *The State of the Planet: Frontiers and Challenges in Geophysics*, *Geophys. Mono. 150*, pp. 147–159. Washington, DC: American Geophysical Union.

Constable S and Constable C (2004b) Observing geomagnetic induction in magnetic satellite measurements and associated implications for mantle conductivity. *Geochemistry, Geophysics, and Geosystems* 5: Q01006. http://dx.doi.org/10.1029/2003GC000634.

Constable SC, Parker RL, and Constable CG (1987) Occam's Inversion: A practical algorithm for generating smooth models from EM sounding data. *Geophysics* 52: 289–300.

Constable S and Roberts JJ (1997) Simultaneous modeling of thermopower and electrical conduction in olivine. *Physics and Chemistry of Minerals* 24: 319–325.

Constable SC, Shankland TJ, and Duba A (1992) The electrical conductivity of an isotropic olivine mantle. *Journal of Geophysical Research* 97: 3397–3404.

Dai L and Karato S (2009a) Electrical conductivity of pyrope-rich garnet at high temperature and high pressure. *Physics of the Earth and Planetary Interiors* 176: 83–88.

Dai L and Karato S (2009b) Electrical conductivity of wadsleyite at high temperatures and high pressures. *Earth and Planetary Science Letters* 287: 277–283.

Didwall EM (1984) The electrical conductivity of the upper mantle as estimated from satellite magnetic field data. *Journal of Geophysical Research* 89: 537–542.

Dobson DP and Brodholt JP (2000) The electrical conductivity of the lower mantle phase magnesiowustite at high temperatures and pressures. *Journal of Geophysical Research* 105: 531–538.

Dosso SE and Oldenburg DW (1991) Magnetotelluric appraisal using simulated annealing. *Geophysical Journal International* 106: 379–385.

Du Frane WL, Roberts JJ, Toffelmier DA, and Tyburczy JA (2005) Anisotropy of electrical conductivity in dry olivine. *Geophysical Research Letters* 32: L24315.

Duba AG, Schock RN, Arnold E, and Shankland TJ (1990) An apparatus for measurement of electrical conductivity to 1500°C at known oxygen fugacity. In: Duba AG, Durham WB, Handin JW, and Wang HF (eds.) *The Brittle-Ductile Transitions in Rocks. The Heard Volume*, *Geophys. Monogr. Ser*, vol. 56, pp. 207–210. Washington, DC: AGU.

Duba AG and Shankland TJ (1982) Free carbon and electrical conductivity in the Earth's mantle. *Geophysical Research Letters* 9: 1271–1274.

Ducea MN and Park SK (2000) Enhanced mantle conductivity from sulfide minerals, southern Sierra Nevada, California. *Geophysical Research Letters* 27: 2405–2408.

Eaton DW and Jones A (2006) Tectonic fabric of the subcontinental lithosphere: Evidence from seismic, magnetotelluric and mechanical anisotropy. *Physics of the Earth and Planetary Interiors* 158: 85–91.

Egbert GD (1997) Robust multiple-station magnetotelluric data processing. *Geophysical Journal International* 130: 475–496.

Egbert GD and Booker JR (1986) Robust estimation of geomagnetic transfer-functions. *Geophysical Journal of the Royal Astronomical Society* 87: 173–194.

Egbert GD and Booker JR (1992) Very long period magnetotellurics at Tucson-observatory – Implications for mantle conductivity. *Journal of Geophysical Research* 97: 15099–15112.

Everett ME and Constable S (1999) Electric dipole fields over an anisotropic seafloor: Theory and application to the structure of 40 Ma Pacific Ocean lithosphere. *Geophysical Journal International* 136: 41–56.

Everett ME, Constable S, and Constable CG (2003) Effects of near-surface conductance on global satellite induction responses. *Geophysical Journal International* 153: 277–286.

Everett ME and Schultz A (1993) 2-Dimensional nonlinear magnetotelluric inversion using a genetic algorithm. *Journal of Geomagnetism and Geoelectricity* 45: 1013–1026.

Everett M and Schultz A (1996) Geomagnetic induction in a heterogeneous sphere, azimuthally symmetric test computations and the response of an u 660-km discontinuity. *Journal of Geophysical Research* 101: 2765–2783.

Filloux JH (1987) Instrumentation and experimental methods for oceanic studies. In: Jacobs JA (ed.) *Geomagnetism*, pp. 143–248. New York: Academic Press.

Gaillard F, Marki M, Iacono-Marziano G, Pichavant M, and Scaillet B (2008) Carbonatite melts and electrical conductivity in the asthenosphere. *Science* 322: 1363–1365.

Gamble TD, Clarke J, and Goubau WM (1979) Magnetotellurics with a remote magnetic reference. *Geophysics* 44: 53–68.

Gill PE, Murray W, and Wright MH (1981) *Practical Optimization*. London: Academic Press.

Grammatica N and Tarits P (2002) Contribution at satellite altitude of electromagnetically induced anomalies arising from a three-dimensional heterogeneously conducting earth, using Sq as an inducing source field. *Geophysical Journal International* 151: 913–923.

Grandis H, Menvielle M, and Roussignol M (1999) Bayesian inversion with Markov chains-I. The magnetotelluric one-dimensional case. *Geophysical Journal International* 138: 757–768.

Hamano Y (2002) A new time-domain approach for the electromagnetic induction problem in a three-dimensional heterogeneous Earth. *Geophysical Journal International* 150: 753–769.

Heinson G and Constable SC (1992) The electrical conductivity of the oceanic upper mantle. *Geophysical Journal International* 110: 159–179.

Heinson GS and White A (2005) Electrical resistivity of the northern Australian lithosphere: Crustal anisotropy or mantle heterogeneity? *Earth and Planetary Science Letters* 232: 157–170.

Hirsch LM (1990) Electrical conduction of Co_2SiO_4. *Physics and Chemistry of Minerals* 17: 187–190.

Hirsch LM and Shankland TJ (1991) Point-defects in (Mg, Fe)SIO_3 perovskite. *Geophysical Research Letters* 18: 1305–1308.

Hirsch LM and Wang CY (1986) Electrical conductivity of olivine during high-temperature creep. *Journal of Geophysical Research* 91: 429–441.

Huang XG, Xu YS, and Karato SI (2005) Water content in the transition zone from electrical conductivity of wadsleyite and ringwoodite. *Nature* 434: 746–749.

Ito E and Takahashi E (1987) Ultrahigh-pressure phase transformations and the constitution of the deep mantle. In: Manghnani MH and Syono Y (eds.) *High-Pressure Research in Mineral Physics*, pp. 221–229. Washington, DC: American Geophysical Union.

Karato S (1990) The role of hydrogen in the electrical conductivity of the upper mantle. *Nature* 347: 272–273.

Key K and Constable S (2011) Coast effect distortion of marine magnetotelluric data: Insights from a pilot study offshore northeastern Japan. *Physics of the Earth and Planetary Interiors* 184: 194–207.

Key K, Constable S, Liu L, and Pommier A (2013) Electrical image of passive mantle upwelling beneath the northern East Pacific Rise. *Nature* 495: 499–502.

Key K and Weiss C (2006) Adaptive finite-element modeling using unstructured grids: The 2D magnetotelluric example. *Geophysics* 71: G291–G299.

Kittel C (1986) *Introduction to Solid State Physics*, sixth edn. New York: Wiley.

Kuvshinov AV, Avdeev DB, and Pankratov OV (1999) Global induction by Sq and Dst sources in the presence of oceans: Bimodal solutions for non-uniform spherical surface shells above radially symmetric earth models in comparison to observations. *Geophysical Journal International* 137: 630–650.

Kuvshinov AV, Avdeev DB, Pankratov OV, Golyshev SA, and Olsen N (2002) Modelling electromagnetic fields in 3-D spherical earth using fast integral equation approach. In: Zhdanov MS and Wannamaker PE (eds.) *Three Dimensional Electromagnetics, Methods in Geochemistry and Geophysics 35*, pp. 43–54. Amsterdam: Elsevier.

Kuvshinov AV and Olsen N (2004) Modelling the coast effect of geomagnetic storms at ground and satellite altitude. In: Reigber C, Luhr H, Schwintzer P, and Wickert J (eds.) *Earth Observation with CHAMP. Results from 'Three Years in Orbit'*, pp. 353–359. Berlin: Springer.

Kuvshinov A and Olsen N (2006) A global model of mantle conductivity derived from 5 years of CHAMP, Orsted, and SAC-C magnetic data. *Geophysical Research Letters* 33: L18301.

Lahiri BN and Price AT (1939) Electromagnetic induction in non-uniform conductors, and the determination of the conductivity of the Earth from terrestrial magnetic variations. *Philosophical Transactions of the Royal Society of London (A)* 237: 509–540.

Laske G and Masters G (1997) A global digital map of sediment thickness. *Eos, Transactions of the American Geophysical Union* 78(46): F483, Fall Meet. Suppl., Abstract S41E-01.

Libermann RC and Wang Y (1992) Characterization of sample environment in a uniaxial split-sphere apparatus. In: Syono Y and Manghnani MH (eds.) *High Pressure Research: Applications to Earth and Planetary Sciences*, pp. 19–31. Washington, DC: American Geophysical Union.

Lizarralde D, Chave A, Hirth G, and Schultz A (1995) Northeastern Pacific mantle conductivity profile from long-period magnetotelluric sounding using Hawaii to California submarine cable data. *Journal of Geophysical Research* 100: 17837–17854.

Mackie RL and Madden TR (1993) 3-Dimensional magnetotelluric inversion using conjugate gradients. *Geophysical Journal International* 115: 215–229.

Marquardt DW (1963) An algorithm for least-squares estimation of non-linear parameters. *Journal of the Society for Industrial and Applied Mathematics* 11: 431–441.

Martinec Z (1999) Spectral-finite element approach to three-dimensional electromagnetic induction in a spherical Earth. *Geophysical Journal International* 136: 229–250.

McCammon C (2005) The paradox of mantle redox. *Science* 308: 807–808.

McDonald KL (1957) Penetration of the geomagnetic secular field through a mantle with variable conductivity. *Journal of Geophysical Research* 62: 117–141.

Mead C and Jeanloz R (1987) High precision strain measurements at high pressures. In: Manghnani MH and Syono Y (eds.) *High-Pressure Research in Mineral Physics*, pp. 41–51. Washington, DC: Am. Geophys. Union.

Medin AE, Parker RL, and Constable S (2006) Making sound inferences from geomagnetic sounding. *Physics of the Earth and Planetary Interiors* 160: 51–59.

Morgan FD, Williams ER, and Madden TR (1989) Streaming potential properties of Westerly Granite with applications. *Journal of Geophysical Research* 94: 12449–12461.

Naif S, Key K, Constable S, and Evans RL (2013) Melt-rich channel observed at the lithosphere-asthenosphere boundary. *Nature* 495: 356–359.

Newman GA and Alumbaugh DL (2000) Three-dimensional magnetotelluric inversion using non-linear conjugate gradients. *Geophysical Journal International* 140: 410–424.

Nielsen OV, Petersen JR, Primdahl F, et al. (1995) Development, construction and analysis of the Orsted fluxgate magnetometer. *Measurement Science and Technology* 6: 1099–1115.

O'Neill HStC (1987) Quartz–fayalite–iron and quartz–fayalite–magnetite equilibria and the free energy of formation of fayalite (Fe_2SioO_4) and magnetite (Fe_3O_4). *American Mineralogist* 72: 67–75.

Oldenburg DW (1983) Funnel functions in linear and non-linear appraisal. *Journal of Geophysical Research* 88: 7387–7398.

Olsen N (1992) Day-to-day c-response estimation for Sq from 1-cpd to 6-cpd using the Z-Y-method. *Journal of Geomagnetism and Geoelectricity* 44: 433–447.

Olsen N (1999) Long-period (30 days–1 year) electromagnetic sounding and the electrical conductivity of the lower mantle beneath Europe. *Geophysical Journal International* 138: 179–187.

Olsen N, Vennerstrøm S, and Friis-Christensen E (2003) Monitoring magnetospheric contributions using ground-based and satellite magnetic data. In: Reigber C, Luehr H, and Schwintzer P (eds.) *First CHAMP Mission Results for Gravity, Magnetic and Atmospheric Studies*, pp. 245–250. Berlin: Springer.

Parker RL (1984) The inverse problem of resistivity sounding. *Geophysics* 49: 2143–2158.

Parker RL (1994) *Geophysical Inverse Theory*. Princeton, NJ: Princeton University Press.

Parker RL and Booker JR (1996) Optimal one-dimensional inversion and bounding of magnetotelluric apparent resistivity and phase measurements. *Physics of the Earth and Planetary Interiors* 98: 269–282.

Parker RL and Whaler K (1981) Numerical methods for establishing solutions to the inverse problem of electromagnetic induction. *Journal of Geophysical Research* 86: 9574–9584.

Parkinson WD (1983) *Introduction to Geomagnetism*. Amsterdam: Elsevier.

Petiau G (2000) Second generation of lead-lead chloride electrodes for geophysical applications. *Pure and Applied Geophysics* 157: 357–382.

Pinheiro K and Jackson A (2008) Can a 1-D mantle electrical conductivity model generate magnetic jerk differential time delays? *Geophysical Journal International* 173: 781–792.

Poe B, Romano C, Nestola F, and Rubie D (2005) Electrical conductivity of hydrous single crystal San Carlos olivine. *Eos, Transactions of the American Geophysical Union* 86(52), Fall Meet. Suppl., Abstract MR41A-0895.

Poe TB, Romano C, Nestola F, and Smyth JR (2010) Electrical conductivity anisotropy of dry and hydrous olivine at 8 GPa. *Physics of the Earth and Planetary Interiors* 181: 103–111.

Quist AS and Marshall WL (1968) Electrical conductances of aqueous sodium chloride solutions from 0 to 800° and at pressures to 4000 Bars. *Journal of Physical Chemistry* 71: 684–703.

Revil A and Glover PW (1997) Theory of ionic-surface electrical conduction in porous media. *Physical Review B* 55: 1757–1773.

Roberts JJ and Tyburczy JA (1999) Partial-melt electrical conductivity: Influence of melt composition. *Journal of Geophysical Research* 104: 7055–7065.

Romano C, Poe BT, Tyburczy J, and Nestola F (2009) Electrical conductivity of hydrous wadsleyite. *European Journal of Mineralogy* 21: 615–622.

Sabaka TJ, Olsen N, and Purucker ME (2004) Extending comprehensive models of the Earth's magnetic field with Orsted and CHAMP data. *Geophysical Journal International* 159: 521–547.

Schmeling H (1986) Numerical models on the influence of partial melt on elastic, anelastic, and electrical properties of rocks. 2. Electrical conductivity. *Physics of the Earth and Planetary Interiors* 43: 123–136.

Schmucker U (1970) Anomalies of geomagnetic variations in the Southwestern United States. *Bulletin of the Scripps Institution of Oceanography* 13: 69.

Schock RN, Duba A, and Shankland TJ (1989) Electrical conduction in olivine. *Journal of Geophysical Research* 94: 5829–5839.

Schultz A, Kurtz RD, Chave AD, and Jones AG (1993) Conductivity discontinuities in the upper mantle beneath a stable craton. *Geophysical Research Letters* 20: 2941–2944.

Schuster A and Lamb H (1889) The diurnal variation of terrestrial magnetism. *Philosophical Transactions of the Royal Society of London* 45: 481–486.

Shankland TJ and Duba AG (1997) Correlation of olivine electrical conductivity change with water activity. *Eos, Transactions of the American Geophysical Union* 78(46), Fall Meet. Suppl., Abstract T52D-10.

Shankland TJ, Duba AG, Mathez EA, and Peach CL (1997) Increase of electrical conductivity with pressure as an indicator of conduction through a solid phase in midcrustal rocks. *Journal of Geophysical Research* 102: 14741–14750.

Simpson F and Bahr K (2005) *Practical Magnetotellurics*. Cambridge: Cambridge University Press.

Simpson F and Tommasi A (2005) Hydrogen diffusivity and electrical anisotropy of a peridotite mantle. *Geophysical Journal International* 160: 1092–1102.

Smith JT and Booker JR (1991) Rapid inversion of 2-dimensional and 3-dimensional magnetotelluric data. *Journal of Geophysical Research* 96: 3905–3922.

Srivastava SP (1966) Theory of the magnetotelluric method for a spherical conductor. *Geophysical Journal of the Royal Astronomical Society* 11: 373–387.

Stacey FD and Anderson OL (2001) Electrical and thermal conductivities of Fe–Ni–Si alloy under core conditions. *Physics of the Earth and Planetary Interiors* 124: 153–162.

Stesky RM and Brace WF (1973) Electrical conductivity of serpentinized rocks to 6 kilobars. *Journal of Geophysical Research* 78: 7614–7621.

Tarits P, Hautot S, and Perrier F (2004) Water in the mantle: Results from electrical conductivity beneath the French Alps. *Geophysical Research Letters* 31: L06612.

Tikhonov AN (1950) Determination of the electrical characteristics of the deep strata of the Earth's crust. *Doklady Akademii NaukSSSR* 73: 295–297.

Tikhonov AN and Arsenin VY (1977) *Solutions of Ill-Posed Problems*. New York: John Wiley and Sons.

Toffelmier DA and Tyburczy JA (2007) Electromagnetic detection of a 410-km-deep melt layer in southwestern United States. *Nature* 447: 991–994.

Tuller HL and Norwick AS (1977) Small polaron electron transport in reduced CeO_2 single crystals. *Journal of Physics and Chemistry of Solids* 38: 859–867.

Tyburczy JA and Roberts JJ (1990) Low frequency electrical response of polycrystalline olivine compacts: Grain boundary transport. *Geophysical Research Letters* 17: 1985–1988.

Tyburczy JA and Waff HS (1983) Electrical conductivity of molten basalt ad andesite to 25 kilobars pressure: Geophysical significance and implications for charge transport and melt structure. *Journal of Geophysical Research* 88: 2413–2430.

Uyeshima M and Schultz A (2000) Geoelectromagnetic induction in a heterogeneous sphere, a new 3-D forward solver using a staggered-grid integral formulation. *Geophysical Journal International* 140: 636–650.

Velimsky J, Everett ME, and Martinec Z (2003) The transient Dst electromagnetic induction signal at satellite altitudes for a realistic 3-D electrical conductivity in the crust and mantle. *Geophysical Research Letters* 30. http://dx.doi.org/10.1029/2002GL016671.

Wang D, Mookherjee M, Xu Y, and Karato S (2006) The effect of water on the electrical conductivity of olivine. *Nature* 443: 977–980.

Watson HC, Roberts JJ, and Tyburczy JA (2010) Effect of conductive impurities on electrical conductivity in polycrystalline olivine. *Geophysical Research Letters* 37: L02302. http://dx.doi.org/10.1029/2009GL041566.

Webb SC, Constable SC, Cox CS, and Deaton T (1985) A seafloor electric field instrument. *Journal of Geomagnetism and Geoelectricity* 37: 1115–1130.

Weidelt P (1972) The inverse problem in geomagnetic induction. *Zeitschrift für Geophysik* 38: 257–289.

Weiss CJ (2001) A matrix-free approach to solving the fully 3D electromagnetic induction problem. In: *Contributed Paper at SEG 71st Annual Meeting, San Antonio, USA*.

Weiss CJ and Everett ME (1998) Geomagnetic induction in a heterogeneous sphere, fully three-dimensional test computation and the response of a realistic distribution of oceans and continents. *Geophysical Journal International* 135: 650–662.

Xu YS, Poe BT, Shankland TJ, and Rubie DC (1998) Electrical conductivity of olivine, wadsleyite, and ringwoodite under upper-mantle conditions. *Science* 280: 1415–1418.

Xu YS and Shankland TJ (1999) Electrical conductivity of orthopyroxene and its high pressure phases. *Geophysical Research Letters* 26: 2645–2648.

Xu YS, Shankland TJ, and Duba AG (2000) Pressure effect on electrical conductivity of mantle olivine. *Physics of the Earth and Planetary Interiors* 118: 149–161.

Yoshimura R and Oshiman N (2002) Edge-based finite element approach to the simulation of geoelectromagnetic induction in a 3-D sphere. *Geophysical Research Letters* 29. http://dx.doi.org/10.1029/2001GL014121.

Yoshino T and Katsura T (2012) Re-evaluation of electrical conductivity of anhydrous and hydrous wadsleyite. *Earth and Planetary Science Letters* 337–338: 56–67.

Yoshino T, Manthilake G, Matsuzaki T, and Katsura T (2008a) Dry mantle transition zone inferred from the conductivity of wadsleyite and ringwoodite. *Nature* 451: 326–329.

Yoshino T, Matsuzaki T, Shatskiy A, and Katsura T (2009) The effect of water on the electrical conductivity of olivine aggregates and its implications for the electrical structure of the upper mantle. *Earth and Planetary Science Letters* 288: 291–300.

Yoshino T, Matsuzaki T, Yamashita S, and Katsura T (2006) Hydrous olivine unable to account for conductivity anomaly at the top of the asthenosphere. *Nature* 443: 973–976.

Yoshino T, McIsaac E, Laumonier M, and Katsura T (2012) Electrical conductivity of partial molten carbonate peridotite. *Physics of the Earth and Planetary Interiors* 194–195: 1–9.

Yoshino T, Nishi M, Matsuzaki T, Yamazaki D, and Katsura T (2008b) Electrical conductivity of majorite garnet and its implications for electrical structure in the mantle transition zone. *Physics of the Earth and Planetary Interiors* 170: 193–200.

Yoshino T, Yamazaki D, Ito E, and Katsura T (2008c) No interconnection of ferro-periclase in post-spinel phase inferred from conductivity measurement. *Geophysical Research Letters* 35: L22303. http://dx.doi.org/10.1029/2008GL035932.

Zhang B, Yoshino T, Wu X, Matsuzaki T, Shan S, and Katsura T (2012) Electrical conductivity of enstatite as a function of water content: Implications for the electrical structure in the upper mantle. *Earth and Planetary Science Letters* 357–358: 11–20.